

## Enhancing the performance of a novel CoRu/CeO<sub>2</sub> bimetallic catalyst for the dry reforming of methane via a mechanochemical process

Marina Armengol-Profitós <sup>a,b</sup>, Andrea Braga <sup>a,b</sup>, Laia Pascua-Solé <sup>a,b</sup>, Ilaria Lucentini <sup>a,b</sup>, Xènia Garcia <sup>a,b,c</sup>, Lluís Soler <sup>a,b,c</sup>, Xavier Vendrell <sup>a,b</sup>, Isabel Serrano <sup>a,b</sup>, Ignacio J. Villar-García <sup>d</sup>, Virgina Pérez-Dieste <sup>d</sup>, Carlos Escudero <sup>d</sup>, Núria J. Divins <sup>a,b,c,\*</sup>, Jordi Llorca <sup>a,b,c,\*</sup>

<sup>a</sup> Institute of Energy Technologies, Universitat Politècnica de Catalunya, EEBE, Eduard Maristany 10-14, 08019 Barcelona, Spain

<sup>b</sup> Department of Chemical Engineering, Universitat Politècnica de Catalunya, EEBE, Eduard Maristany 10-14, 08019 Barcelona, Spain

<sup>c</sup> Barcelona Research Center in Multiscale Science and Engineering, Universitat Politècnica de Catalunya, EEBE, Eduard Maristany 10-14, 08019 Barcelona, Spain

<sup>d</sup> ALBA Synchrotron Light Source, Carrer de la Llum 2-26, Cerdanyola del Vallès, 08290 Barcelona, Spain



### ARTICLE INFO

#### Keywords:

Mechanochemistry  
Methane dry reforming (DRM)  
Operando characterization  
Bimetallic catalyst  
Hydrogen production

### ABSTRACT

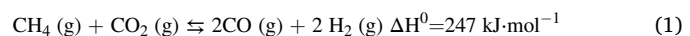
A mechanochemical synthesis method has been used to synthesize CoRu nanoparticles supported on CeO<sub>2</sub> for methane dry reforming. In this work, we study the effect of Ru addition to Co/CeO<sub>2</sub>-based catalysts and of the synthesis method by screening their catalytic activity, using synchrotron X-ray diffraction (XRD), and *operando* near-ambient pressure X-ray photoelectron spectroscopy (NAP-XPS). Ruthenium addition directly impacts the reducibility of cobalt species and results in smaller particle sizes, as demonstrated by H<sub>2</sub>-temperature programmed reduction and XRD. NAP-XPS shows that Ru modifies the metal-support interaction, as evidenced by the higher Ce<sup>3+</sup>/Ce ratios for the bimetallic samples and tuning the oxidation state of Ru. The synthesis method also influences the dispersion of Co and Ru on the surface. Mechanochemically-prepared samples (mono- and bimetallic) outperformed the conventionally-synthesized counterparts by reaching higher CH<sub>4</sub> and CO<sub>2</sub> conversions, resulting in a stable CoRu/CeO<sub>2</sub> catalyst for 24 h at 700 °C and yielding an H<sub>2</sub>/CO ratio close to 1.

### 1. Introduction

Methane is the main component of natural gas, being the simplest hydrocarbon that exists. It is a very stable molecule (C-H bond energy  $\Delta H^\circ=440 \text{ kJ}\cdot\text{mol}^{-1}$ ) and it has a high calorific heat ( $C_p=35.7 \text{ J}\cdot\text{K}^{-1}\cdot\text{mol}^{-1}$ ) [1]. Methane is a powerful greenhouse gas with a warming potential 28 times higher than that of CO<sub>2</sub> [2].

The conversion of natural gas or biogas, whose main component is methane and represents a renewable alternative, into other chemicals can increase its added value. Different oxidising agents for methane conversion can be chosen, such as oxygen in methane partial oxidation, carbon dioxide in the dry reforming (DRM, reaction 1), or water vapour in the steam reforming (MSR). Since the 1960 s, MSR has been the main process for producing synthesis gas (syngas, a mixture of hydrogen and carbon monoxide), which may be used as a first step in the Fischer-Tropsch (FT) process, or for hydrogen production. Noteworthy, the reaction of methane with CO<sub>2</sub> (DRM) to produce syngas is an opportunity

for converting two greenhouse gases, while revalorizing CO<sub>2</sub> emissions [3]. Furthermore, the produced syngas normally has lower quantities of CO<sub>2</sub> and an H<sub>2</sub>/CO ratio close to 1 compared to MSR (H<sub>2</sub>/CO ratio of 3) [1], which is desirable for the FT process or aldehydes production.

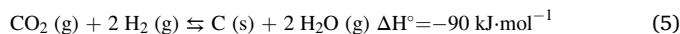
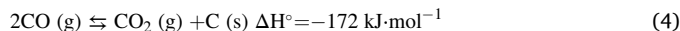
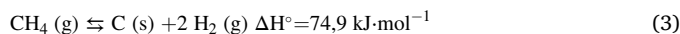
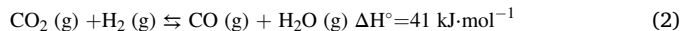


DRM has 20% lower operational costs than other reforming processes [4], nevertheless it is an endothermic reaction, that requires the activation of two stable molecules. Normally, the operating temperature range is between 650 and 1000 °C. In addition, it involves several secondary reactions that are intrinsically related to the operational temperature. These secondary reactions lead to H<sub>2</sub> consumption through the reverse water-gas shift reaction (RWGS) (2) and to coke formation through methane decomposition (3), Boudouard reaction (4), CO<sub>2</sub> (5) and CO reduction (6). The Boudouard reaction is hindered at temperatures above 700 °C [5], but carbon deposition is thermodynamically feasible up to 870 °C with a feed ratio of CO<sub>2</sub>/CH<sub>4</sub> = 1:1 [6]. At high

\* Corresponding authors at: Institute of Energy Technologies, Universitat Politècnica de Catalunya, EEBE, Eduard Maristany 10-14, 08019 Barcelona, Spain.

E-mail addresses: [nuria.jimenez.divins@upc.edu](mailto:nuria.jimenez.divins@upc.edu) (N.J. Divins), [jordi.llorca@upc.edu](mailto:jordi.llorca@upc.edu) (J. Llorca).

temperatures, it has been observed that the carbon species formed are more reactive and the gasification rate of coke is equivalent to or faster than the coke formation, resulting in a lower net deposition [5]. Nevertheless, high temperatures commonly lead to thermal sintering of the metal particles.



Industrially, nickel-based catalysts are commonly used and Ni is one of the most investigated metals. Nevertheless, deactivation due to carbon deposition or sintering, low CO<sub>2</sub> activation, and compatibility with a green feedstock such as biogas impede the industrial implementation of DRM [3].

In this regard, supports have an important role in the enhancement of the activity, selectivity, and stability of catalysts. Cerium dioxide is a promising material with stable sites for the incorporation of metal nanoparticles (NPs) and has redox properties [7]. The basic behaviour of ceria favours CO<sub>2</sub> adsorption and hydrogenation while disfavouring CH<sub>4</sub> activation [8]. Investigations over Ni/CeO<sub>2</sub> catalysts showed improved stability against deactivation despite having less conversion of both reactants compared to Ni/Al<sub>2</sub>O<sub>3</sub> catalysts [9]. Besides, density-functional theory (DFT) calculations have shown that CH<sub>4</sub> activation is strongly related to the metal-CeO<sub>2</sub> interface, facilitating high metal oxidation states and providing highly reducible sites for methane activation [10]. The formulation and methodology used to incorporate the active phase (one or various metals in bimetallic systems) onto the CeO<sub>2</sub> lattice have also been reported to have a direct impact on the metal-support interaction [11] and also on the metal-metal interactions, which have an impact in the catalytic performance [12].

Studies on cobalt-based catalysts have shown that the Co-CeO<sub>2</sub> interaction decreases the formation energy of oxygen vacancies, which play an important role in the CO<sub>2</sub> dissociative adsorption [13], and it modifies the electronic state of metallic Co NPs, resulting in higher activity [7,14]. Cobalt-based catalysts show certain coke resistance due to the higher affinity between cobalt and oxygen species [15–17]. The deactivation mechanism over Co-based catalysts shows a correlation with the metal loading of the catalyst: high cobalt loadings (>12 wt%) have shown notable carbon accumulation, while low content (<2 wt%) facilitate the oxidation of metallic Co species [18]. Besides, the particle size has been unravelled as an important parameter for the Co-support interaction: smaller particles exhibit a stronger interaction, leading to improved activity and stability [19]. The support effect has also been widely investigated for Co-based catalysts and different carbon deposition mechanisms have been identified depending on the nature of the support [20].

The performance of noble metal-based (NM) catalysts has also been thoroughly studied. At 650 °C, the activity of NM catalysts supported on MgAl<sub>2</sub>O<sub>4</sub> ranges: Ru > Rh ≈ Ni > Ir > Pt > Pd, thereby Ru-based catalysts are the most promising catalysts among NM-based. For instance, Ru supported on MgO has been found to have higher selectivity and minimal coke formation than other noble metals like Pd, Ir or Pt [21]. Ruthenium supported on SiO<sub>2</sub> and Y-Al<sub>2</sub>O<sub>3</sub> revealed similar conversions but different evolution under time-on-stream (TOS) due to higher carbon deposition and additional CO<sub>2</sub> consumption for the Al<sub>2</sub>O<sub>3</sub> support, resulting in a lower selectivity [22]. In parallel, doping SiO<sub>2</sub> with CeO<sub>2</sub> decreased the reduction temperature of supported RuO<sub>2</sub> [23]. Besides, Ru nano-clusters (<1 nm) supported on CeO<sub>2</sub> proved to tune the electronic properties of Ru, causing a partially oxidized state of ruthenium stabilized by reduced ceria, differing from large Ru nanoparticles

supported on ceria [24].

Developing bimetallic catalysts by doping Co catalysts with a second metal (M), especially a NM, creating a Co-M interaction, can significantly enhance the activity and coke resistance due to a change of the O<sup>\*</sup> binding strength [25–27]. In this regard, Pt addition to a Co/CeO<sub>2</sub> catalyst resulted in a more active catalyst with a higher H<sub>2</sub>/CO ratio between 500 and 800 °C than the corresponding monometallic catalysts [28]. Ruthenium addition to Ni-based catalysts has been investigated and a direct effect in carbon formation has been established, as the presence of the NM stabilizes metallic Ni species and promotes carbon gasification, decreasing coke deposition [29]. Also, the presence of the noble metal favours the hydrogen spillover effect [30]. Despite the high catalytic performance of Ru-based catalysts and the beneficial effect of Ru-doping in Ni-based catalysts, to the best of our knowledge, bimetallic CoRu/CeO<sub>2</sub> catalysts have not been studied for DRM. CoRu/CeO<sub>2</sub> catalysts have been studied for the Fischer-Tropsch process and a H<sub>2</sub> spillover effect was also described owing to the remarkable interaction between both metals [31].

In contrast to the conventional approach of preparing catalysts by impregnation, in this work, a mechanochemical method has been explored: ball-milling (BM). It has been demonstrated that ball-milling can induce mechanical activation, which is frequently accompanied with an increase in reactivity caused by changes in the structural properties of a material [12], by creating defects in the crystalline structure, and/or creating new types of metal-support interactions [11, 32,33]. Activity, stability and deactivation of active sites can be strongly enhanced by these changes, which can take place both on the surface and in the bulk structure [34]. The mechanochemical synthesis, which is a simple and solvent-free synthesis method, has been demonstrated to be effective in the reduction of pollutants generated during fossil fuel combustion, like soot oxidation over CeO<sub>2</sub> catalysts [35] or methane oxidation over Pd/CeO<sub>2</sub> [11,36,37]. Regarding DRM, Pd/CeO<sub>2</sub> via mechanochemical synthesis stands out for its high selectivity [38].

In this work, we developed a series of mono- and bimetallic CoRu/CeO<sub>2</sub> catalysts and investigated the effects of their mechanochemical synthesis using physicochemical characterization and in situ techniques to unravel the distinct features created during the milling process that differ from conventionally-impregnated catalysts. By using the same techniques, we also examined the influence of Ru addition to Co/CeO<sub>2</sub> catalysts.

## 2. Experimental

### 2.1. Catalyst preparation

A series of mono- and bimetallic Co and Ru ceria-supported catalysts with a metal loading of 10 wt% of cobalt or/and 1.5 wt% of ruthenium were synthesized. The cerium dioxide (ceria) was synthesized following a precipitation method using cerium nitrate (Ce(NO<sub>3</sub>)<sub>3</sub>·6 H<sub>2</sub>O, Alfa Aesar) and NH<sub>3</sub> as precipitating agent. An aqueous NH<sub>3</sub> solution (28% w/w) was added under vigorous stirring until a pH of 10 was reached. The precipitate was aged overnight and, subsequently, it was washed thoroughly and filtered. The resulting cake was dried at 105 °C and calcined at 950 °C for 5 h. Cobalt and Ru were added following two different methods: incipient wetness impregnation (IWI) and ball milling (BM). Cobalt acetate (Co(CH<sub>3</sub>COO)<sub>2</sub>·4 H<sub>2</sub>O, VWR) and ruthenium chloride (RuCl<sub>3</sub>, TCI Chemicals) were used as metal precursors.

For the mechanochemical synthesis, a mini-mill Pulverisette 23 (Fritsch) operated at 50 Hz for 15 min was used. The synthesis consisted of loading the ceria powder and the Co and/or Ru precursors in a 15 ml ZrO<sub>2</sub> grinding jar with three balls of the same material (10 mm of diameter and 3 g of weight each to obtain a ball-to-powder weight ratio -BPR- of 10). After the preparation, the milled powder was calcined in static air at 450 °C (5°C/min of heating rate) for 4 h.

The same catalysts were prepared via a conventional incipient wetness impregnation (IWI) method. An aqueous solution with one or

both metal precursors was prepared and added dropwise to the calcined ceria in several steps, drying them at 105 °C between impregnations. Once the whole solution was incorporated, the impregnated materials were calcined in static air at 450 °C for 4 h (5°C/min). To investigate the impact of the mechanochemical synthesis, two additional bimetallic catalysts were synthesized: (i) a CoRu catalyst was prepared by milling CeO<sub>2</sub> at 50 Hz for 15 min, followed by the incipient wetness impregnation of the metal precursors and calcination procedures previously described. This catalyst has been named CoRu/(CeO<sub>2</sub>-M)-IWI. (ii) A catalyst named (CoRu/CeO<sub>2</sub>-IWI)-M, where a milling step (50 Hz and 15 min) was done after the incipient wetness impregnation of the metal precursors and before the calcination process. No CeOCl phase has been detected by XRD and HRTEM.

## 2.2. Characterization

Temperature-programmed reduction (TPR) experiments were carried out in a ChemStar TPx system. The samples (75 mg) were pre-treated with Ar at 450 °C (10 °C/min) for 10 min and the reduction was performed from room temperature (RT) up to 950 °C with a flow of 10% H<sub>2</sub>/Ar (50 ml/min total flow) with a heating ramp of 10 °C/min and holding at 950 °C for 25 min.

High-resolution transmission electron microscopy (HRTEM) and scanning transmission electron microscopy (STEM) were carried out on a FEI Tecnai F20 instrument equipped with a field emission electron source operated at 200 kV. Catalysts after activation in hydrogen were also studied. The treatment consisted of a reduction at 400 °C (10 °C/min) for 1 h in 10% H<sub>2</sub>/N<sub>2</sub> followed by a passivation by cooling down freely in N<sub>2</sub> and flowing 2% O<sub>2</sub>/N<sub>2</sub> once room temperature was reached for 30 min.

Raman spectroscopy was performed in a confocal equipment (Renishaw in Via Qontor), equipped with a Leica DM2700M microscope (50x magnification). A 532-nm laser excitation was used and all spectra were normalized to CeO<sub>2</sub> peak at 464 cm<sup>-1</sup>.

Thermogravimetric analyses (TGA) were performed using a Q500 instrument from TA Instruments. The analyses were performed from room temperature to 900 °C (10 °C/min) with 50 ml/min of synthetic air and loading 13–30 mg of spent catalyst.

The metal loading was quantified by inductively coupled plasma-optical emission spectrometry (ICP-OES, Perkin Elmer Optima 3200RL). The digestion procedure of the samples to perform ICP-OES was done in a Zr crucible with 1 g of sodium hydroxide, 1 g of sodium nitrate and 50 mg of each sample, melted at 600 °C. Then, a 10% HCl (v/v) solution was used to dissolve the resulting melts. The solutions were added into 250 ml volumetric flasks and filled to the mark with 10% HCl (v/v) solution in order to transform Ru into a stable chloro-complex [39].

In situ synchrotron X-ray diffraction (SXRD) measurements were carried out at beamline BL-04 MSPD and BL-16 NOTOS of the ALBA Synchrotron (Cerdanyola del Vallès, Barcelona, Spain), to investigate the evolution of the catalysts during the reduction treatment and reaction. The measurements were performed with an energy corresponding to a wavelength of  $\lambda = 0.412 \text{ \AA}$  and  $\lambda = 0.558 \text{ \AA}$ , respectively. To perform the measurements, the catalysts were loaded in quartz capillaries of 0.58 mm inner diameter (ID) and a wall thickness of 300 μm. Firstly, inert gas (argon) was flowed through the sample and diffractograms at RT were acquired. Then, the BM sample was reduced in situ from RT to 400 °C (10 °C/min), with 5 ml/min of 5% H<sub>2</sub>/He holding the temperature at 400 °C for 1 h. The reduction of the IWI sample was performed directly at 400 °C for 1 h with the same hydrogen mixture, after increasing the temperature under an Ar flow. The samples were heated up using a hot blower. The crystallite size was calculated with the Scherrer Eq. (7), where d is the crystallite size (nm);  $\lambda$  is the X-ray wavelength (nm); FWHM is the full width at half maximum of the diffraction peak at  $\theta$ , and  $\theta$  is the diffraction angle.

$$d = \frac{0.9 \cdot \lambda}{FWHM \cdot \cos\theta} \quad (7)$$

Near-ambient pressure X-ray photoelectron spectroscopy (NAP-XPS) measurements were performed at the CIRCE beamline of the ALBA Synchrotron (BL-24), which is equipped with a Phoibos NAP150 detector from SPECS GmbH (10 eV pass energy and 0.1 eV step size were used to analyze the catalysts). The catalysts were pressed on gold meshes. The sample temperature was controlled using an infrared laser ( $\lambda = 808 \text{ nm}$ ) focused on a stainless-steel plate on top of which the samples were mounted. The temperature was monitored during all the experiments with a K-type thermocouple in direct contact with the samples. The series of measurements consisted of: (i) an oxidation step under 1 mbar of O<sub>2</sub> at 450 °C (10 °C/min) for 1 h to remove adventitious carbon; (ii) an activation step under 1 mbar of H<sub>2</sub> for 1 h at 400 °C to reduce the catalysts; (iii) DRM reaction (reaction mixture CO<sub>2</sub>:CH<sub>4</sub> = 1:1, dosing 2 ml/min of each reactant gas) under 1 mbar at 550 °C and (iv) DRM at 700 °C (10 °C/min used as heating ramps). When switching from H<sub>2</sub> to DRM conditions, the bimetallic samples were kept at 400 °C, H<sub>2</sub> was pumped out, and then 2 ml/min CH<sub>4</sub> and 2 ml/min CO<sub>2</sub> were dosed until 1 mbar was reached. Once the mixture was stabilized, the sample temperature was increased to 550 °C. For the monometallic samples, the reactants dosing was performed at 550 °C to prevent oxidation of the sample at low reaction temperatures. Cerium 3d, Co 2p, O 1 s, Ru 3p, Ru 3d, and C 1 s spectral regions were acquired with two different photon energies to generate photoelectrons of two kinetic energies (KE) in order to extract information from two different depths and be able to obtain depth profiles: (i) with KE = 215 eV to prove the surface (ca. 0.6 nm of inelastic mean free path -IMFP- for Co 2p and Ru 3d) and (ii) KE = 450 eV for the subsurface (ca. 0.9 nm of IMFP for Co 2p and Ru 3d). In Table S1, the IMFP and the photon energies used for each element and region are detailed. CasaXPS was used for data analysis. The spectra were calibrated for energy taking into account the theoretical position of the  $u''''$  peak of the Ce 3d<sub>3/2</sub>, which was set at binding energy (BE) = 916.8 eV [40]. The Co 2p<sub>3/2</sub> region of metallic cobalt (Co<sup>0</sup>) has a main peak at a BE of about 778.1 eV, which can be deconvoluted with an asymmetric peak and two plasmon loss peaks (bulk and surface) above the main peak [41]. These two peaks are centred at 5.0 and 3.0 eV above the asymmetric metallic peak. The theoretical BE differences and the ratio between areas of these three components were used to fit Co<sup>0</sup>. Co<sup>2+</sup> in CoO has a BE of 781 eV with a strong satellite, more pronounced than in Co<sub>3</sub>O<sub>4</sub>, at a BE between 3.7–6.1 eV above the main peak [42]. Co<sub>3</sub>O<sub>4</sub> is composed of one-third of Co<sup>2+</sup> (tetrahedral environment) and two-thirds of Co<sup>3+</sup> (octahedral environment) and can be deconvoluted with five peaks, where the first one is at 779.6 eV. Therefore, when Co is composed of a mixture of oxidized states, the deconvolution using the theoretical peaks becomes impractical. Consequently, to determine the oxidation state of Co regions with a mixture of oxides and metallic Co, experimental lines corresponding to CoO and Co<sub>3</sub>O<sub>4</sub> were created. The BE range of these experimental lines was fixed and kept constant throughout the experiments and a linear background was subtracted. The line corresponding to CoO was created with CoRu/CeO<sub>2</sub>-IWI sample at 550 °C during DRM and the one corresponding to Co<sub>3</sub>O<sub>4</sub> with Co/CeO<sub>2</sub>-BM sample during the O<sub>2</sub> treatment at 450 °C. The full width at half maximum (FWHM) was kept equal to 1 for all the deconvolutions when the experimental lines were used. Near-edge X-ray absorption fine structure (NEXAFS) spectra of Co-L<sub>3</sub>/L<sub>2</sub> edge was also acquired during the experiments. The deconvolution of the Ce 3d region was performed with six peaks for Ce<sup>4+</sup> corresponding to three pairs of spin-orbit doublets and four peaks for Ce<sup>3+</sup>, which correspond to two doublets [43]. Ruthenium 3d region superimposes the C 1 s and Ce 4s core level. Additionally, the contribution of the gas phase with three peaks corresponding to methane at 286.2 eV, one peak corresponding to CO<sub>2</sub> at 293 eV and one peak corresponding to CO at 291.8 eV are also present in the Ru 3d region. Ruthenium 3d peaks corresponding to the metallic specie are deconvoluted considering a doublet with a main asymmetric

peak at 279.9 eV and a spin-orbit splitting (SOS) of 4.17 eV [44]. For the oxide species, RuO<sub>2</sub> peaks have been experimentally determined at 280.9 eV with the corresponding satellites approximately at 1.8 eV above each component [45]. Atomic fractions of Ce, Co and Ru were obtained from the peak areas corrected for the incident photon flux, and the corresponding cross-sections [46]. The gaseous atmosphere was analysed by a quadrupole mass spectrometer Microvision 2 Residual Gas Analyzer (MKS Instruments) installed in the second stage of the differential pumping system of the analyser.

### 2.3. Catalytic performance tests

Catalytic activity tests were performed using a Microactivity Effi Solo equipment (Process Integral Development Eng & Tech). Quartz reactors (ID = 10 mm) were filled with 200 mg of sample diluted with silicon carbide (Alfa Aesar, 46 grit) with a mass ratio of 12 for a total volume of 1.5 cm<sup>3</sup>. Prior to the reaction tests, the catalysts were activated inside the quartz reactors under a 10% H<sub>2</sub> in N<sub>2</sub> stream for one hour at 400 °C (heating rate of 5 °C/min). For the DRM reaction tests, a total gas flow of 120 ml/min of the reactants mixture with a molar concentration of CO<sub>2</sub>: CH<sub>4</sub>:N<sub>2</sub> = 1:1:4 (N<sub>2</sub> was used as an internal standard) to reach a gas hourly space velocity (GHSV) of 4800 h<sup>-1</sup> was dosed. The DRM tests were performed between 550 and 950 °C, at intervals of 50 °C where the reaction conditions were kept constant for 45 min to allow enough time to reach the steady state. A condenser was used to condense water vapour. The gaseous effluent from the reactor was analysed using a micro-gas chromatograph (490 Micro GC from Agilent Technologies), equipped with a molecular sieve 5 Å and a PoraPlot U column. The microGC was connected online to the reactor effluent and the concentration was analysed every four min. Only H<sub>2</sub> and CO were detected in the gaseous effluent.

Conversion (X, Eq. 8) and selectivity (S, Eq. 9) were calculated, where  $\dot{n}_{i,IN}$  and  $\dot{n}_{i,OUT}$  are the inlet and outlet molar flows of the species *i* (mol/min).

$$X_i = \frac{\dot{n}_{i,IN} - \dot{n}_{i,OUT}}{\dot{n}_{i,IN}} \cdot 100 \quad (8)$$

$$S_{H_2} = \frac{\dot{n}_{H_2,OUT}}{\dot{n}_{H_2,OUT} + \dot{n}_{CO,OUT}} \cdot 100; \quad (9)$$

The catalytic tests for samples CoRu/CeO<sub>2</sub>-BM and CoRu/CeO<sub>2</sub>-IWI were repeated three times to evaluate the reproducibility of the results. The dispersion of the results is represented in the activity plots with the error bars.

Stability tests were carried out during 24 h at 700 °C under the same flow and gas hourly space velocity as for the catalytic tests. The analysis of the outlet stream was done every 20 min using the same microGC. The spent catalyst was separated from the SiC by sieving the catalytic bed using a 200 µm sieve in order to characterize the post-reaction samples.

The turnover frequency of H<sub>2</sub> formation was calculated from the number of active sites estimated by Eq. 10 [47], where *D* is the metal dispersion,  $v_m$  is the bulk atomic volume of the metal,  $a_m$  is the surface area occupied by an atom on a polycrystalline surface, and  $d_{VA}$  is the average particle size. In this study, the nanoparticle size was determined by XRD and spherical particles were assumed.

$$D = 6 \cdot \frac{\left( \frac{v_m}{a_m} \right)}{d_{VA}} \quad (10)$$

## 3. Results

### 3.1. Catalyst characterization

The chemical composition of all catalysts was determined by ICP-OES and the results are listed in Table S2. The Co concentration is close to the nominal concentration, being slightly lower for the IWI samples than for the BM counterparts, indicating that the precursors can be loaded more efficiently on the ceria support with the mechanochemical synthesis.

Representative HRTEM and STEM images of the catalysts after the reduction and passivation process are displayed in Fig. 1 while Fig. S1 shows the images of the calcined (as-prepared) catalysts. After reduction and passivation, the monometallic Co/CeO<sub>2</sub>-IWI catalyst shows well-dispersed Co<sub>3</sub>O<sub>4</sub> NPs over the ceria surface of 9 ± 3 nm (Fig. 1 A-B). In the passivated monometallic Co/CeO<sub>2</sub>-BM catalyst (Fig. 1 E-G), two types of NPs are identified: on one hand, Co<sub>3</sub>O<sub>4</sub> NPs of ca. 8 nm, and on the other, NPs of 11 ± 5 nm displaying a core-shell of oxidation states are also distinguished, as seen in Fig. 1 F. The NPs show a core of metallic Co fcc and a Co<sub>3</sub>O<sub>4</sub> shell, as inferred from the planes at 2.05 Å and 1.77 Å, corresponding to (111) and (200) planes of Co fcc, and at 2.89 Å corresponding to (220) of Co<sub>3</sub>O<sub>4</sub>. This indicates that the extent of the oxidation after the passivation and air exposure is limited to the first layers of the NPs, which is not the case for the Co/CeO<sub>2</sub>-IWI catalyst (Fig. 1 A-B).

In the reduced and passivated CoRu/CeO<sub>2</sub>-IWI catalyst (Fig. 1 D), small NPs dispersed over ceria are seen. The large crystallite visible in Fig. 1 D shows reflections at 3.14 and 1.92 Å corresponding to CeO<sub>2</sub> (111) and (220) planes. The NPs supported on it display planes at 3.17 and 2.47 Å corresponding to (110) and (101) planes of tetragonal RuO<sub>2</sub>, and at 2.37 Å, which correspond to Co<sub>3</sub>O<sub>4</sub> (311). The average NPs size is 10.4 nm.

The bimetallic catalysts show a clearly different morphology depending on the synthesis method: the mechanochemical synthesis creates an amorphous layer surrounding the ceria crystallites and defined Co NPs (Fig. 1 H-J). The width of the layer is ca. 2 nm, as seen in Fig. 1 I, and no reflections are detected from this layer due to its amorphous nature. This layer has been previously observed on mechanochemically synthesised Pd-CeO<sub>2</sub> and PdPt-CeO<sub>2</sub> catalysts [11,36,37]. CoRu/CeO<sub>2</sub>-BM also shows NPs displaying planes at 2.44 Å corresponding to (311) planes of the cobalt spinel as well as metallic Co NPs, where both Co hcp and Co fcc phases are present, as planes at 1.91 Å and 2.05 Å, which correspond to Co hcp (101) and Co fcc (111), respectively, are identified. No Ru NPs are identified on the catalyst. Nevertheless, the presence of Ru is confirmed with EDX analyses, as evidenced in the spectrum shown of the NP analysed in Fig. 1 H.

In the monometallic Ru/CeO<sub>2</sub>-BM, ca. 10 nm NPs without planes are observed in Fig. 1 K. In Fig. 1 L, the two large NPs identified show reflections at 1.69 Å and 2.06 Å, which correspond to (211) planes of RuO<sub>2</sub> and (101) planes of metallic Ru. Additionally, NPs of ca. 1–3 nm can be seen at the edge of CeO<sub>2</sub> crystals (Fig. 1 K, marked with arrows) that can be ascribed to Ru NPs due to the different contrast observed with the ceria crystallites.

### 3.2. Temperature-programmed-reduction (TPR)

Fig. 2 and Table S3 show the hydrogen consumption for Co, Ru and CoRu catalysts prepared by BM and IWI during temperature-programmed reduction (TPR) experiments. An effect in the reducibility of Co species upon Ru addition and the effect of the synthesis method can be clearly seen, as the samples show notable changes of the redox properties. As reported elsewhere [48], TPR of cobalt spinel (Co<sub>3</sub>O<sub>4</sub>) typically presents two peaks at 300 and 367 °C. The first peak at low-temperature is associated with the reduction of Co<sup>3+</sup> ions to Co<sup>2+</sup> with the structural change to CoO, while the peak at higher temperature is related to the CoO reduction to metallic cobalt. The reduction peak

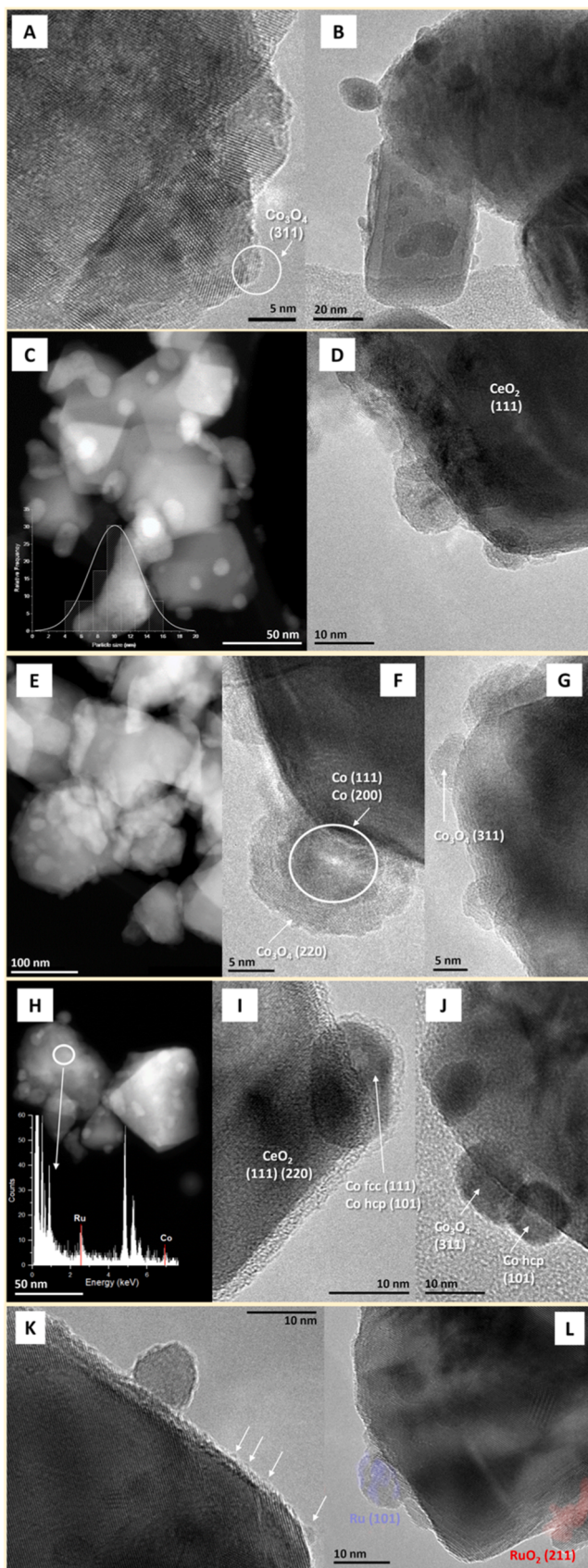


**Fig. 1.** TEM and STEM images of Co/CeO<sub>2</sub>-IWI (A-B), CoRu/CeO<sub>2</sub>-IWI (C-D), Co/CeO<sub>2</sub>-BM (E-G), CoRu/CeO<sub>2</sub>-BM (H-J) and Ru/CeO<sub>2</sub>-BM (K-L) after the reduction and passivation process.

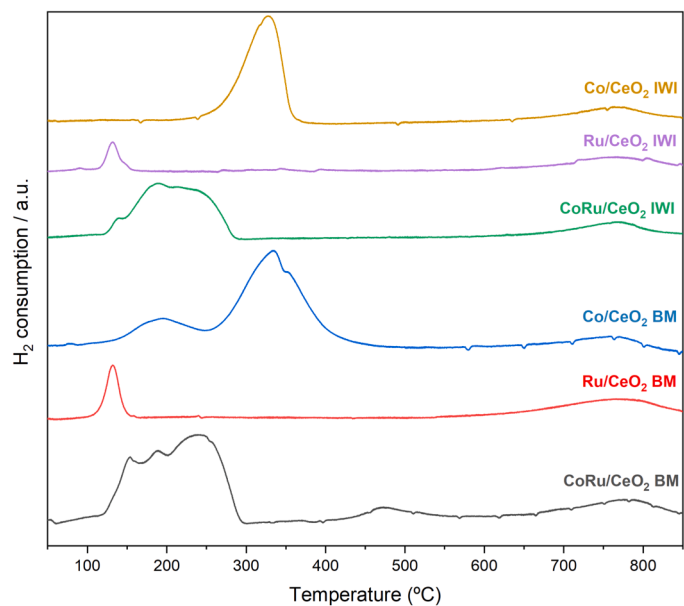


**Fig. 2.** TPR of monometallic and bimetallic IWI and BM catalysts.

observed at ca. 320 °C indicates that in Co/CeO<sub>2</sub>-IWI, Co is mainly present in the form of the spinel that reduces consuming 1846 μmol H<sub>2</sub>/g<sub>cat</sub>. On the other hand, Co/CeO<sub>2</sub>-BM shows two peaks: a peak at low-temperature with onset temperature at ca. 190 °C that can indicate the reduction of more superficial Co<sup>2+</sup> or smaller NPs, and a peak at ca. 320 °C consuming a total amount of hydrogen of 1241 μmol/g<sub>cat</sub>.

The reduction of ruthenium oxide occurs at 140 °C (reduction of Ru<sup>4+</sup> to Ru<sup>0</sup>) in the Ru/CeO<sub>2</sub>-BM and IWI samples as well as in the bimetallic samples. The monometallic Ru catalysts show the same hydrogen consumption at lower temperature (263 μmol H<sub>2</sub>/g<sub>cat</sub>), while the H<sub>2</sub> consumption of the CeO<sub>2</sub> peak is higher for the Ru/CeO<sub>2</sub>-BM catalyst, suggesting an effect of the milling process in the CeO<sub>2</sub> reduction.

Both bimetallic samples, IWI and BM, show peaks at temperatures lower than 300 °C, clearly decreasing the reduction temperature of Co species, which indicates that Ru addition increases the reducibility of Co species. Hydrogen consumption values suggest a slightly higher reduction degree for the ball-milled sample.

In the ball-milled bimetallic sample (CoRu/CeO<sub>2</sub> BM), a new peak at 470 °C appears, which can be ascribed to the reduction of the CeO<sub>2</sub> surface [49]. The peak at a higher temperature (770 °C), present in all the samples, corresponds to the reduction of the ceria bulk. The H<sub>2</sub> consumption associated with the peaks corresponding to CeO<sub>2</sub> reduction reflects that the CoRu/CeO<sub>2</sub>-BM exhibits the highest degree of reduction. When comparing the different samples, the reduction degree can be ranked as follows: Ru/CeO<sub>2</sub>-BM > CoRu/CeO<sub>2</sub>-IWI > Co/CeO<sub>2</sub>-IWI ~ Ru/CeO<sub>2</sub>-IWI ~ Co/CeO<sub>2</sub>-BM.

### 3.3. Synchrotron XRD measurements

All as-prepared samples (Fig. S2) show the presence of diffraction peaks at d-spacings that correspond to those of cerium dioxide. Peaks corresponding to Co<sub>3</sub>O<sub>4</sub> are present in mono- and bimetallic Co and CoRu catalysts (d-spacings of 2.45 Å, 2.35 Å and 2.04 Å), except for Co/CeO<sub>2</sub>-BM, which only presents peaks corresponding to the CoO crystalline structure (2.48 Å and 2.14 Å). The bimetallic samples also show peaks corresponding to tetragonal RuO<sub>2</sub> (2.53 Å), with low intensity in the case of CoRu/CeO<sub>2</sub>-IWI. Monometallic Ru/CeO<sub>2</sub>-IWI and BM samples show the presence of RuO<sub>2</sub>, in the same way as bimetallic catalysts, but at 2.56 Å and 1.69 Å (Fig. S2). The shift observed in the d-spacing values for the Ru peaks indicates that some cobalt is inserted in the

structure of the ruthenium oxide.

The Co crystallite sizes calculated using the Scherrer equation for the as-prepared samples are shown in Table S4. The  $\text{CeO}_2$  crystallite size at room temperature is slightly different between samples depending on the synthesis method: 71 nm for IWI catalysts and 65 nm for the BM ones. Monometallic  $\text{Co}/\text{CeO}_2$ -IWI catalyst has a remarkably higher crystallite size than the BM counterpart. The addition of ruthenium has a direct impact on Co crystallite size, decreasing the size of Co crystallites by more than 50%.

The evolution of the crystalline structure for  $\text{CoRu}/\text{CeO}_2$  samples during a reduction under  $\text{H}_2$  was monitored by in situ synchrotron XRD (SXRD) (Fig. S3, table S4). A gradual reduction of  $\text{Co}_3\text{O}_4$  to  $\text{CoO}$  starts, followed by the reduction of  $\text{CoO}$  to metallic Co hcp and fcc.  $\text{CoRu}/\text{CeO}_2$ -IWI undergoes the same phase changes resulting in a mixture of  $\text{CeO}_2$ , metallic Co (hcp and fcc), and metallic Ru after 1 h under  $\text{H}_2/\text{He}$  at 400 °C (Fig. S4). During the  $\text{H}_2$  reduction, there are no signs of alloy in Co in the bimetallic catalysts, as inferred from the position and symmetry of the metallic Co peaks. The reduction sequence observed with the transformation of  $\text{Co}_3\text{O}_4$  to  $\text{CoO}$  and finally to Co agrees with the TPR results.

### 3.4. Catalytic performance test

Fig. 3 shows methane and carbon dioxide conversion and the selectivity at each temperature for the six catalysts investigated. Table S5 lists

the  $\text{CH}_4$  and  $\text{CO}_2$  conversions and the normalized  $\text{H}_2$  production per gram of metal at 700 °C. Comparing the impregnated catalysts, the monometallic  $\text{Co}/\text{CeO}_2$ -IWI is the least active catalyst among the ones tested and the monometallic  $\text{Ru}/\text{CeO}_2$ -IWI catalyst shows higher  $\text{CH}_4$  and  $\text{CO}_2$  conversion. A strong enhancement of the catalytic activity for the bimetallic  $\text{CoRu}/\text{CeO}_2$ -IWI formulation is observed: methane and  $\text{CO}_2$  conversion increase by ca. 50% and 30%, respectively, with respect to  $\text{Ru}/\text{CeO}_2$ -IWI. Additionally, the  $\text{H}_2/\text{CO}$  ratio is favourably affected by Ru addition as  $\text{CoRu}/\text{CeO}_2$ -IWI reaches a ratio of 1.0 at 700 °C, compared with 0.57 of the  $\text{Co}/\text{CeO}_2$ -IWI or 0.87 of the  $\text{Ru}/\text{CeO}_2$ -IWI.

Interestingly, the ball milling synthesis has a clear impact on the catalytic performance. A dramatic increase for both the  $\text{CH}_4$  and  $\text{CO}_2$  conversions is observed for the BM counterparts, irrespective of the composition, being the enhancement of  $\text{CH}_4$  and  $\text{CO}_2$  conversions more prominent for  $\text{Ru}/\text{CeO}_2$ -BM and  $\text{CoRu}/\text{CeO}_2$ -BM. In fact, the monometallic  $\text{Ru}/\text{CeO}_2$ -BM catalyst shows the highest  $\text{CH}_4$  and  $\text{CO}_2$  conversions among the monometallic samples and its performance is close to that obtained by  $\text{CoRu}/\text{CeO}_2$ -BM, which is the catalyst reaching the highest  $\text{CH}_4$  and  $\text{CO}_2$  conversions: at 700 °C,  $\text{CoRu}/\text{CeO}_2$ -BM reaches 71%  $\text{CH}_4$  conversion and 81%  $\text{CO}_2$  conversion. Fig. S12 shows the results of the activity tests for the  $\text{CoRu}/(\text{CeO}_2\text{-M})$ -IWI and  $(\text{CoRu}/\text{CeO}_2\text{-IWI})\text{-M}$  samples in addition to the  $\text{CoRu}/\text{CeO}_2$ -BM sample. Milling the precursors together with ceria leads to higher  $\text{CO}_2$  conversions for all the temperature range studied and to higher  $\text{CH}_4$  conversions at temperatures above 650 °C.

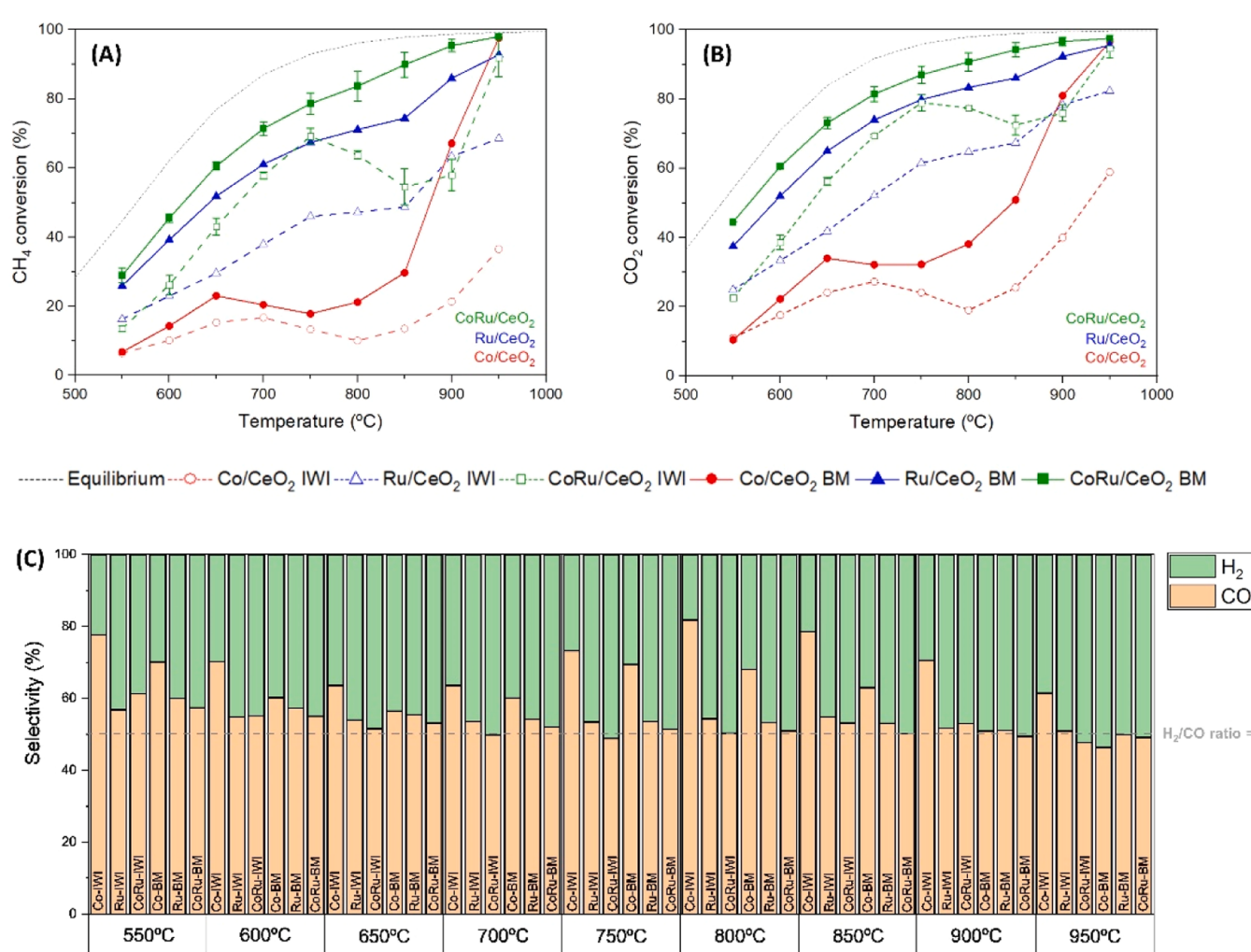


Fig. 3. Effect of the temperature on the  $\text{CH}_4$  (A) and  $\text{CO}_2$  conversion (B), and  $\text{H}_2$  and  $\text{CO}$  selectivity (C) for the IWI and BM catalysts ( $\text{GHSV} = 4800 \text{ h}^{-1}$  and  $\text{WHSV} = 36000 \text{ ml} \cdot \text{h}^{-1} \cdot \text{g}_{\text{cat}}^{-1}$ ).

Another important effect of the milling method is on catalysts' stability, which was investigated for 24 h at 700 °C (Fig. 4): CoRu/CeO<sub>2</sub>-BM and Ru/CeO<sub>2</sub>-BM show a steady behaviour on both CH<sub>4</sub> and CO<sub>2</sub> conversions, while Co/CeO<sub>2</sub>-IWI and CoRu/CeO<sub>2</sub>-IWI show a decrease of the conversions, indicating a gradual deactivation of the catalysts. Monometallic Co catalysts show their typical deactivation [38] and the conversion of both reactants sharply decreases during the first hours of the experiment, leading to the complete deactivation of the IWI catalyst after 5 h under time-on-stream (TOS). Conversely, Co/CeO<sub>2</sub>-BM also shows an initial deactivation period of ca. 5 h and after that, it reaches stable CH<sub>4</sub> and CO<sub>2</sub> conversions at 10% and 9%, respectively, which remain constant during the rest of the 24 h test. For the monometallic Ru catalysts, this deactivation is less drastic and they retain higher conversions than the monometallic Co catalysts after 24 h of reaction. The Ru/CeO<sub>2</sub>-IWI catalyst even shows a slight increase of the CH<sub>4</sub> conversion after 10 h under reaction, indicating an activation under TOS. Nevertheless, the H<sub>2</sub>/CO ratio at 1 h is lower than one and it decreases after 24 h under TOS (Fig. 4b), indicating an increase in the extent of the reverse water-gas shift reaction, thereby decreasing the H<sub>2</sub> production. Comparing these results with the ones obtained for Ru/CeO<sub>2</sub>-BM, the effect of the synthesis method is also remarkable after the 24 h under TOS in terms of conversion (Figs. 4a and 4b), as well as of selectivity (Fig. 4c). While for Ru/CeO<sub>2</sub>-IWI the H<sub>2</sub>/CO ratio decreases to 0.37 after 24 h under TOS, in the ball-milled counterpart it increases to 0.85. Noteworthy, Ru/CeO<sub>2</sub>-BM attains 80% and 73% CH<sub>4</sub> and CO<sub>2</sub> conversion, respectively, which doubles the conversions obtained by the IWI catalysts and its performance is stable during the whole test. Furthermore, the catalytic performance of Ru/CeO<sub>2</sub>-BM is superior to that of a traditionally synthesized CoRu/CeO<sub>2</sub>-IWI and it has the highest H<sub>2</sub> production rate per gram of metal among the catalysts tested (16322 mmolH<sub>2</sub>·h<sup>-1</sup>·g<sup>-1</sup>, see Table S5). Turnover frequency (TOF)

values of the bimetallic catalysts have been calculated, being 1.1 s<sup>-1</sup> for the ball-milled sample and 0.7 s<sup>-1</sup> for the IWI sample, assuming both Co and Ru as active sites.

The CoRu/CeO<sub>2</sub>-BM and Ru/CeO<sub>2</sub>-BM are the catalysts showing the highest performance, being the bimetallic CoRu/CeO<sub>2</sub>-BM catalyst the best one among the catalysts tested. After 24 h under TOS, the bimetallic milled catalyst converts 80% methane in comparison with 73% methane conversion of Ru/CeO<sub>2</sub>-BM, and the H<sub>2</sub>/CO ratio is 0.99. The methane conversion of CoRu/CeO<sub>2</sub>-BM represents an increase of 40%, with a CO<sub>2</sub> conversion of 86%, compared with its traditionally synthesised counterpart; CoRu/CeO<sub>2</sub>-IWI has a conversion of 42% and 54% of CO<sub>2</sub> and CH<sub>4</sub>, respectively, at the end of the test.

### 3.5. Transmission Electron Microscopy after reaction

Co/CeO<sub>2</sub>-IWI, CoRu/CeO<sub>2</sub>-IWI, Co/CeO<sub>2</sub>-BM and CoRu/CeO<sub>2</sub>-BM samples after the temperature reaction tests (activity data shown in Fig. 3) were investigated by TEM and the images are presented in Fig. 5. Morphological differences between CoRu/CeO<sub>2</sub>-BM and IWI are observed: the BM bimetallic sample shows a layer surrounding the ceria crystallites after reaction. The width of the layer is around 7 nm (see images 5 H and 5I), wider than before reaction (Fig. 1I). A closer inspection shows that there are reflections at 2.9 Å that can correspond to the (220) plane of cobalt spinel, revealing a rearrangement of Co NPs in the form of small aggregates of NPs smaller than 5 nm in close contact with ceria crystallites, thus revealing that in the milled sample Co NPs cluster together and no massive sintering takes place. The presence of Ru in these aggregates cannot be excluded. Isolated bimetallic CoRu NPs were also identified, such as the CoRu NP displayed in Fig. 5J, as determined by EDX analyses (see inset), where an intense Ru peak, as well as Co peaks, were obtained. This NP also displays Co<sub>3</sub>O<sub>4</sub> planes. In

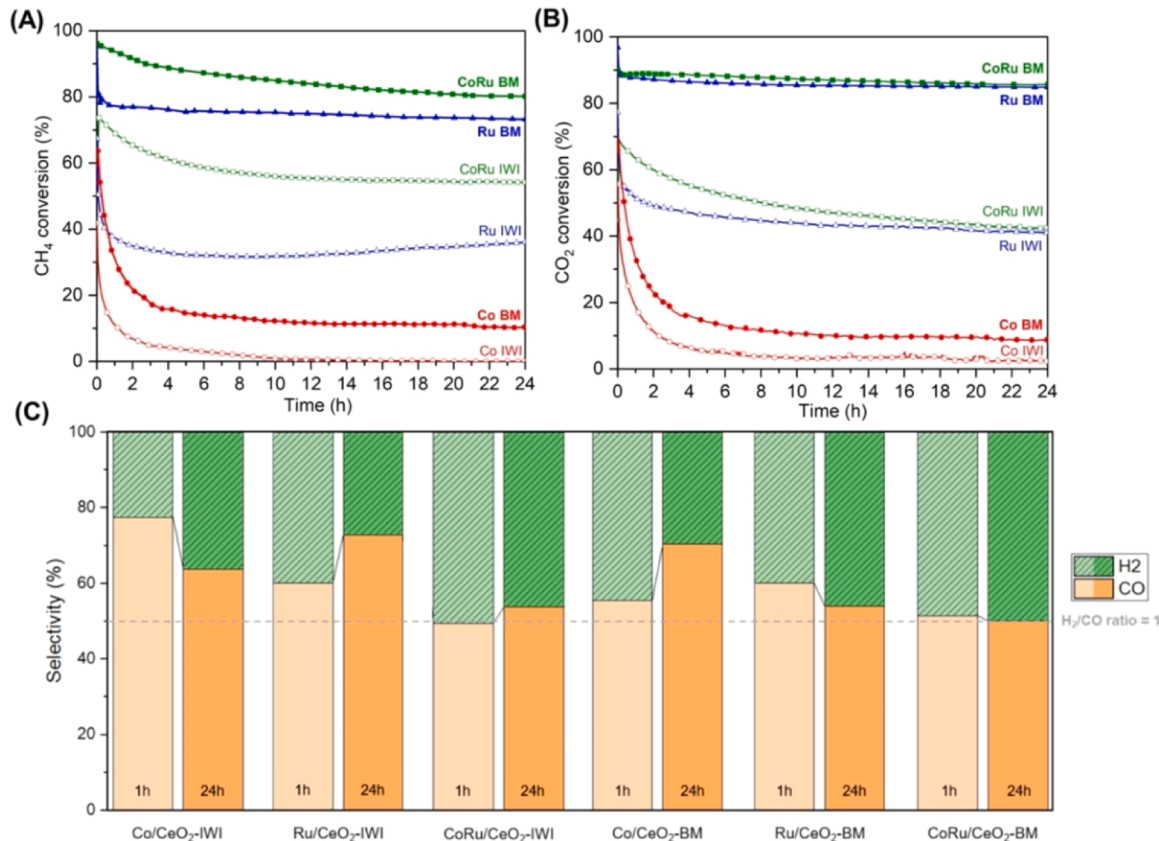


**Fig. 4.** Evolution of CH<sub>4</sub> (A) and CO<sub>2</sub> conversion (B) during 24 h of stability test at 700 °C for the IWI and BM catalysts. Selectivity after 1 h and 24 h under TOS (C). (GHSV=4800 h<sup>-1</sup> and WHSV=36 000 ml·h<sup>-1</sup>·g<sub>cat</sub><sup>-1</sup>).

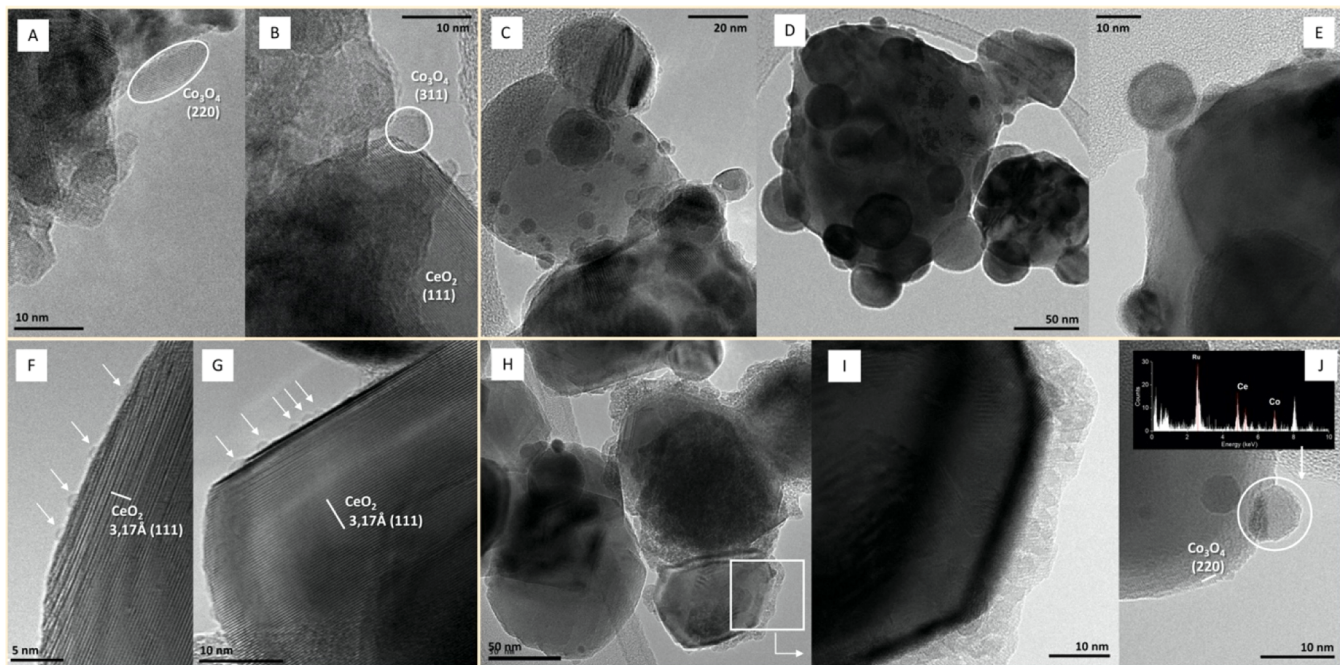


**Fig. 5.** TEM images of Co/CeO<sub>2</sub>-IWI (A-B), CoRu/CeO<sub>2</sub>-IWI (C-E), Co/CeO<sub>2</sub>-BM (F-G) and CoRu/CeO<sub>2</sub>-BM (H-J) after reaction.

clear contrast, the CoRu/CeO<sub>2</sub>-IWI catalyst shows big agglomerations (25 nm) around all the CeO<sub>2</sub> crystals, indicating sintering of Co and/or Ru NPs (Fig. 5D) due to the reaction conditions tested. These agglomerates coexist with smaller NPs of ca. 5 nm that show planes at 2.15 Å, corresponding to (200) plane of CoO (Fig. 5C).

The morphology of the monometallic samples is also greatly influenced by the synthesis method. Co/CeO<sub>2</sub>-IWI shows large NPs of ca. 42 nm cobalt spinel as inferred from the (220) and (311) planes of Co<sub>3</sub>O<sub>4</sub>. On the other hand, Co/CeO<sub>2</sub>-BM (Figs. 5F and 5G) shows NPs from 1 to 3 nm on the CeO<sub>2</sub> crystals. These results show that the milling method not only results in smaller NPs on the as-synthesized catalysts but that the NPs retain higher dispersion and smaller sizes during reaction, leading to higher catalytic activity and stability.

### 3.6. Raman spectroscopy

Raman measurements were conducted on the catalysts after the 24 h

stability tests to study the formation of carbonaceous deposits. As seen in Fig. 6, CoRu/CeO<sub>2</sub>-IWI, Ru/CeO<sub>2</sub>-BM and CoRu/CeO<sub>2</sub>-BM catalysts show bands at ca. 1350 and 1585 cm<sup>-1</sup>, which correspond to D and G bands, respectively, suggesting carbon deposition on the surface of the catalysts. D bands are associated with defective and amorphous carbon, while the G band indicates the presence of an ordered carbon structure (graphitic). The amorphous carbon is its most reactive form, while the graphitic form is the least one and causes catalysts' deactivation faster [50].

Comparing the bimetallic catalysts, the ball-milled sample has a higher amount of amorphous carbon than the IWI one. This can justify the greater stability of the mechanochemically synthesised CoRu/CeO<sub>2</sub>-BM as compared to CoRu/CeO<sub>2</sub>-IWI. The presence of these bands is not observed in the Co monometallic catalysts (IWI and BM) due to their low activity and fast deactivation. Similar results are obtained for Ru/CeO<sub>2</sub>-IWI catalyst, despite being more active than the monometallic Co catalysts.

### 3.7. Operando NAP-XPS

To shed light on the surface oxidation state and its reorganization, it was monitored under reaction by NAP-XPS. During the initial oxidation at 450 °C, all species are heavily oxidized, being both Ru and Co fully oxidized (Fig. S5), as expected. During the reduction at 400 °C (Figs. 7 and S6), Ce 3d spectra of monometallic and bimetallic IWI-synthesized catalysts show clear differences in the reduction degree of Ce (Fig. S6), as inferred from the Ce<sup>4+</sup>/Ce ratios shown in Table S8. The Ce 3d spectra during reduction (Fig. S6A and D) show a slightly lower amount of Ce<sup>4+</sup> for the bimetallic formulation than for the monometallic one, 53% vs. 58%, respectively. This difference is larger for the milled catalysts (Fig. S6G and J); the bimetallic sample shows 49% of Ce<sup>4+</sup> while in the monometallic it increases to 60%.

Under reaction conditions, two distinct trends are observed depending on the reaction temperature. At low temperatures (550 °C), the Ce<sup>4+</sup> ratio is higher in the bimetallic samples than in the monometallic counterparts. This can be correlated with the higher CO<sub>2</sub> conversion levels reached by the two bimetallic catalysts in contrast to the monometallic ones (see Fig. 3). Additionally, our results reveal that the

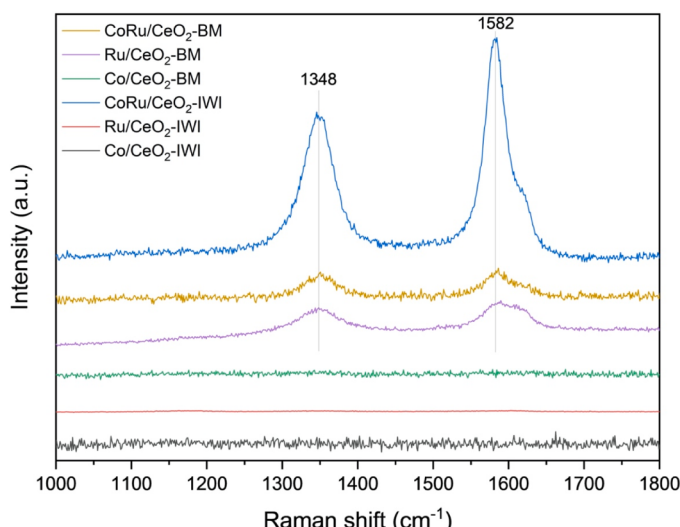


**Fig. 6.** Normalized Raman spectra of all the catalysts after 24 h under TOS.

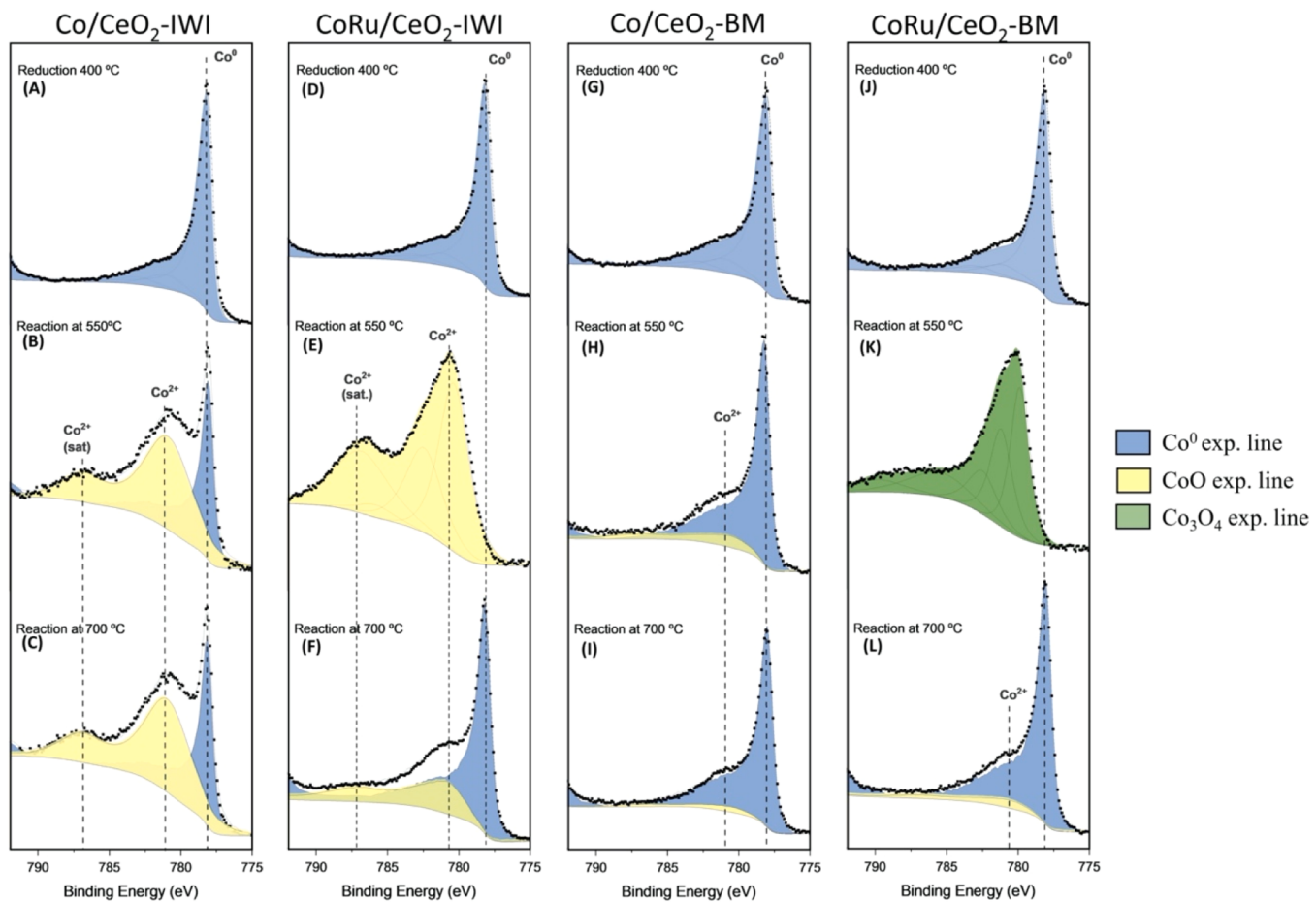


**Fig. 7.** NAP-XPS spectra of the Co 2p region of Co/CeO<sub>2</sub> and CoRu/CeO<sub>2</sub> catalysts, IWI and BM, under 1 mbar H<sub>2</sub> at 400 °C and under CH<sub>4</sub>:CO<sub>2</sub> mixture at 1 mbar at 550 and 700 °C, scans obtained with a KE of 215 eV.

presence of Ru further promotes CO<sub>2</sub> activation and, thus, its conversion. At 700 °C, a different scenario appears and the Ce<sup>4+</sup> ratio decreases sharply. At higher temperatures, methane conversion takes place to a larger extent, thus producing more H<sub>2</sub>, together with an increase of the CO<sub>2</sub> conversion resulting in higher local concentrations of H<sub>2</sub> and CO on the catalysts' surface causing a drop of the Ce<sup>4+</sup> species. This is further confirmed by the sharp increase of reaction products detected in the mass spectrometer interfaced with the analysis chamber (Fig. S7). During DRM at 700 °C, CoRu/CeO<sub>2</sub>-BM shows a slightly higher amount of Ce<sup>4+</sup> than the IWI counterpart. Thus, the synthesis method also has an impact on the maintenance of these oxygen vacancies, consistent with previous works on the use of this mechanical synthesis to induce stress and changes in the surface of CeO<sub>2</sub> [11].

Regarding the oxidation state of cobalt and ruthenium, a competitive behaviour is observed between the activation of CO<sub>2</sub>, which causes the metals' oxidation, and the activation of CH<sub>4</sub>, which reduces them [51]. Besides, the interpretation of Co spectra is not simple because of the binding energy (BE) overlap of metallic and oxidized species and their satellites [42,56]. The Co 2p NAP-XP spectra for the outermost layers (acquired with 215 eV KE) are shown in Figs. 7 and S8 and the corresponding subsurface spectra are shown in Fig. S8. Ru 3d and C 1s regions of the two bimetallic catalysts are shown in Fig. S9 (surface) and Fig. S10 (subsurface). Fig. 8 shows a graphic representation of the atomic fractions and oxidation states calculated for all Co-monometallic and bimetallic catalysts.

Firstly, with regard to the monometallic samples, during the oxidation performed at 450 °C, they completely oxidized and only Co<sub>3</sub>O<sub>4</sub> formation was detected (Fig. S5), while during reduction under H<sub>2</sub> at 400 °C they underwent complete reduction (Fig. 7 A and G). Even

though the monometallic catalysts were kept in vacuum up to 550 °C, upon dosing the reaction mixture at 550 °C, Co<sup>2+</sup> peaks at the outermost layers of Co/CeO<sub>2</sub>-IWI catalyst noticeably developed, resulting in a mixture of metallic Co and CoO (Fig. 7 B). At 550 °C, Co was eminently oxidized as the Co<sup>2+</sup>/Co ratio was 68% and 63% at the surface and subsurface regions, respectively (Fig. 8 O). At 700 °C, the oxidation state of Co remained constant (66% of Co<sup>2+</sup> at the surface) (Fig. 8 P). These results are supported by NEXAFS spectra (Fig. S11). A completely different scenario appears for the milled Co/CeO<sub>2</sub>-BM catalyst: during DRM at both temperatures, the concentration of Co oxide species was below 15% (Fig. 7 H and I). These results show the great impact of the synthesis method on the oxidation state of Co during the reaction: from having ca. 30% of Co in metallic state at the surface of the IWI catalyst to nearly 90% of metallic Co in the BM one. Having a more reduced surface can be responsible for the higher catalytic performances achieved by the BM as metallic Co has been identified as the active species for DRM [38]. Our results show that the mechanochemical synthesis method stabilizes metallic Co under reaction conditions.

In the bimetallic samples, Co<sub>3</sub>O<sub>4</sub> and RuO<sub>2</sub> were detected during the oxidation at 450 °C. During the reduction at 400 °C (Fig. 7 D and J for Co and Fig. S9A and D for Ru), Co and Ru of both samples were fully reduced. As a result of switching to DRM conditions, at 550 °C both samples are oxidized, forming RuO<sub>2</sub> and CoO for the CoRu/CeO<sub>2</sub>-IWI and, surprisingly, Co<sub>3</sub>O<sub>4</sub> for CoRu/CeO<sub>2</sub>-BM. Despite being the metals oxidized, the mass spectrometer showed an increase in the partial pressure of the reaction products (H<sub>2</sub> and CO) (Fig. S7), indicating that the catalysts were active at this temperature. The oxidation observed can be a result of the catalytic performance at low temperature, in agreement with the results obtained for Ce 3d, where CO<sub>2</sub> activation takes

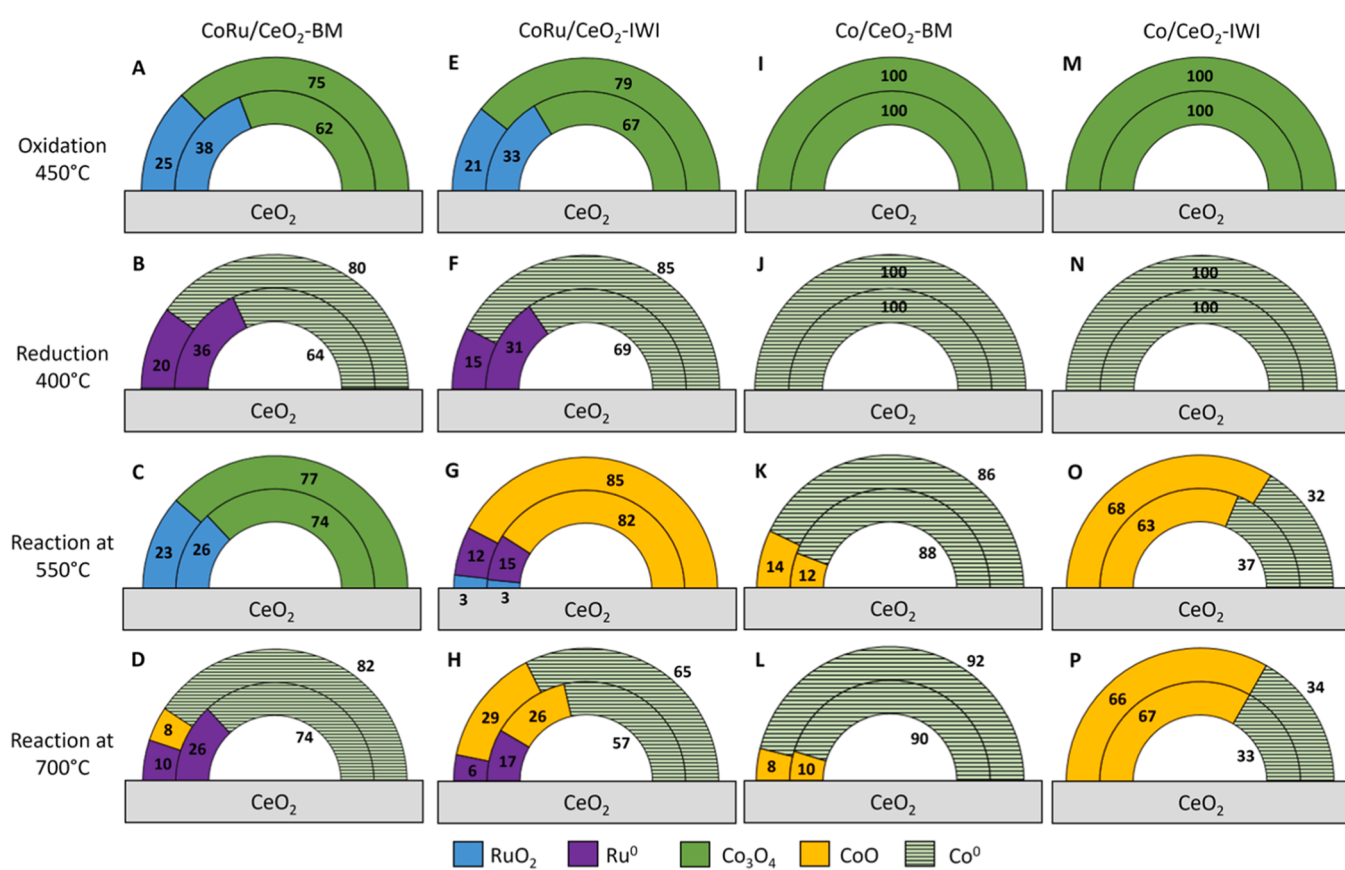


**Fig. 8.** Cobalt and ruthenium atomic fractions and oxidation states extracted from NAP-XPS results for Co/CeO<sub>2</sub> and CoRu/CeO<sub>2</sub> catalysts prepared by IWI and BM, under oxidation conditions at 450 °C, under 1 mbar H<sub>2</sub> at 400 °C and under CH<sub>4</sub>:CO<sub>2</sub> mixture at 1 mbar at 550 and 700 °C, scans obtained with a KE of 215 eV (surface) and 450 eV (subsurface).

place to a larger extent. In fact, the higher CO<sub>2</sub> conversion observed for CoRu/CeO<sub>2</sub>-BM can be responsible for its complete oxidation under reaction at low temperature. When the temperature was raised to 700 °C, Co in both samples underwent a strong reduction. Nevertheless, CoRu/CeO<sub>2</sub>-IWI shows the presence of almost 30% CoO at the outermost layers (Fig. 8 H). In contrast, under the same conditions, CoRu/CeO<sub>2</sub>-BM (Fig. 8 D) shows only 8% CoO.

Different reorganization of the novel metal was obtained for the two bimetallic samples (Table S10). CoRu/CeO<sub>2</sub>-BM sample has a higher amount of Ru present on the surface and subsurface regions compared to the bimetallic IWI sample during DRM. Some sintering took place when increasing the reaction temperature, as the Ru/Ce ratio at the outermost layers decreased from 0.39 to 0.15 in CoRu/CeO<sub>2</sub>-BM and from 0.55 to 0.17 in CoRu/CeO<sub>2</sub>-IWI (Table S10).

#### 4. Discussion

From the results described above it is clear that the ball milling synthesis has a strong impact on the catalytic performance of Co-Ru supported over CeO<sub>2</sub>. To our best knowledge, the combination of the two metals with the CeO<sub>2</sub> support has not been tested before for the dry reforming of methane. Some other supports have been investigated for the CoRu system, such as SiO<sub>2</sub> or TiO<sub>2</sub>, [25], [53] even though, ball-milling was not examined. Also, Co and Ni monometallic, as well as other bimetallic combination, supported on CeO<sub>2</sub> have been studied [23, 24, 28, 52, 54–58].

The influence of Ru addition and the synthesis method in the redox properties of the catalyst have been revealed by TPR. The effect of the addition of a noble metal has been described before for NiRu bimetallic

catalysts supported on Y-Al<sub>2</sub>O<sub>3</sub> for the DRM, ascribing the promotion of Ni reduction upon the noble metal addition to an electronic effect and a hydrogen spillover phenomenon [59]. Therefore, our results indicate a strong interaction between Co and Ru, synthesized both by IWI and BM. This interaction is also confirmed by the shift observed in the d-spacing values for the Ru peaks in the XRD results (Fig. S2), indicating that some cobalt is inserted in the structure of ruthenium oxide in both bimetallic samples. The existence of CoRu bimetallic NPs in CoRu/CeO<sub>2</sub>-BM is also revealed from EDX measurements on the region displayed in Fig. 1H, where both Co and Ru signals were obtained from the same particle. Changes caused by the milling process in the bimetallic CoRu/CeO<sub>2</sub>-BM sample are revealed by TPR. The peak that appears at 490°C (Fig. 2) (seen in several samples analogously synthesized) indicates a change in the structure of the ceria support due to the mechanochemical process. It is known that the milling process can contribute to create defects on the surface or tune the metal-support interaction [11], resulting in a higher ability of reduction, which in combination with Ru addition results in a ceria surface reduction peak at ca. 490°C. This agrees with the NAP-XPS results and could be the reason for the slightly smaller Ce<sup>4+</sup>/Ce ratio observed during reduction at 400°C for the surface of the CoRu-/CeO<sub>2</sub>-BM. As reflected in Fig. S13 just milling the support or the result of the impregnation (the two control samples) does not result in such peak, indicating that both the order of the milling process and the milling with Ru affect the CeO<sub>2</sub> structure.

X-ray diffractograms also show that the mechanochemical process has an effect on reducing the ceria crystallite size from 71 nm for CoRu/CeO<sub>2</sub>-IWI to 65 nm for CoRu/CeO<sub>2</sub>-BM. This effect is also noticeable in the cobalt crystallite sizes in the monometallic Co/CeO<sub>2</sub>-BM catalyst, where the mean Co crystallite size is 13 nm in contrast to 41 nm for Co/

$\text{CeO}_2$ -IWI. The addition of ruthenium has a direct impact on the Co crystallites size as well, decreasing the size of Co crystallites by more than 50%. This is in line with one of the most known effects of noble metal addition to Ni-based systems, where the addition of noble metals leads to smaller metal particles with a higher dispersion due to the dilution effect [50].

A dramatic increase for both  $\text{CH}_4$  and  $\text{CO}_2$  conversions is observed for the BM catalysts, irrespective of the composition, being the enhancement of  $\text{CH}_4$  and  $\text{CO}_2$  conversions more prominent for Ru/ $\text{CeO}_2$ -BM and CoRu/ $\text{CeO}_2$ -BM. In fact, the monometallic Ru/ $\text{CeO}_2$ -BM catalyst shows the highest  $\text{CH}_4$  and  $\text{CO}_2$  conversions among the monometallic samples and its performance is close to that obtained by CoRu/ $\text{CeO}_2$ -BM, which is the catalyst reaching the highest  $\text{CH}_4$  and  $\text{CO}_2$  conversions: at 700 °C, CoRu/ $\text{CeO}_2$ -BM reaches 71%  $\text{CH}_4$  conversion and 81%  $\text{CO}_2$  conversion.

Monometallic Co/ $\text{CeO}_2$  catalysts show the lowest  $\text{H}_2$  selectivity. The methane conversion achieved by the monometallic catalysts is the lowest, thus resulting in lower  $\text{H}_2$  production. In addition, the RWGS could also play a role, consuming part of the produced  $\text{H}_2$  with  $\text{CO}_2$  to form CO. A remarkable synergic effect between both metals is observed at temperatures above 650 °C. The bimetallic CoRu catalysts reach  $\text{H}_2/\text{CO}$  ratios closer to 1 for both synthesis methods. This indicates that the addition of Ru favours methane conversion thereby increasing the  $\text{H}_2$  production. The same effect has also been described in a CoPt/ $\text{CeO}_2$  catalyst, where according to DFT calculations, the presence of the two metals increases the abundance of  $\text{O}^*$  on the surface, enhancing the reforming reaction. This observation can be correlated with our Ce 3d XPS results, where we obtained lower  $\text{Ce}^{4+}$  ratios for the CoRu catalysts (Fig. S6 and Table S8).

The deactivation of the monometallic catalysts obtained during the stability tests (Fig. 4) varied drastically with the addition of the noble metal and with the synthesis method. Co/ $\text{CeO}_2$ -IWI sample completely deactivate after 6 h of TOS, while Co/ $\text{CeO}_2$ -BM maintain some activity after the 24 h. Raman spectra of these catalysts after reaction showed no carbon deposition due to their low catalytic activity. Therefore, the deactivation of both monometallic samples can be likely attributed to sintering of the Co NPs. TEM images demonstrate that the milling process leads to NPs that maintain smaller sizes and greater dispersion throughout the reaction. Moreover, Co NPs in Co/ $\text{CeO}_2$ -BM (Fig. 1F) remain partly metallic after a passivation process in contrast with the IWI counterpart, having both NPs of similar sizes, which can indicate a stronger interaction between the NPs and the support. Ru/ $\text{CeO}_2$  samples exhibit less deactivation than the Co-monometallic samples, which is consistent with the ability to maintain Ru in its metallic state at 700°C, as shown in Figs. 8 and S9. Moreover, carbon deposition can also be responsible for part of the deactivation according to TGA results, a low amount of carbon deposition ( $0.2 \text{ mg}_{\text{carbon}} \cdot \text{g}_{\text{cat}}^{-1} \cdot \text{h}^{-1}$ ) has been found in Ru/ $\text{CeO}_2$ -BM sample after the 24 h stability test that can be related to its high stability. A strong deactivation trend is visible in the CoRu/ $\text{CeO}_2$ -IWI sample at the beginning of the stability test. TGA results showed higher amounts of C ( $22.5 \text{ mg}_{\text{carbon}} \cdot \text{g}_{\text{cat}}^{-1} \cdot \text{h}^{-1}$ ) on this sample than on Ru/ $\text{CeO}_2$ -BM. Sintering of the Co and/or Ru NPs as inferred from TEM images (Fig. 5D) could add to the deactivation observed during the stability test. CoRu/ $\text{CeO}_2$ -BM sample shows a stronger deactivation for  $\text{CH}_4$  conversion than for  $\text{CO}_2$ . Some mechanistic studies have suggested a bifunctional reaction mechanism where  $\text{CH}_4$  dissociation takes place on the transition metals (Ni, or Co in our study), while activation of  $\text{CO}_2$  takes place in the noble metal in bimetallic NiIn/ $\text{Al}_2\text{O}_3$  catalysts [60]. Considering this mechanism, the stronger deactivation observed for methane activation could be due to the limited sintering of the Co NPs as observed in TEM images Fig. 5H-I, which leads to a lower number of active sites for  $\text{CH}_4$  dissociation. Additionally, as seen in Fig. 8, the CoO atomic fraction in CoRu/ $\text{CeO}_2$ -BM is the lowest one, which could also be responsible for the higher activity achieved by this catalyst. After 24 h under TOS,  $11.9 \text{ mg}_{\text{carbon}} \cdot \text{g}_{\text{cat}}^{-1} \cdot \text{h}^{-1}$  carbon deposition was obtained, revealing lower carbon deposition than in the IWI-counterpart. From

Raman spectra analyses, an estimation of the degree of graphitization of the carbon deposits can be performed as well by calculating the ratio between the integrated areas of the D and G bands,  $I_D/I_G$  (results listed in Table S7). It can be seen that Ru/ $\text{CeO}_2$ -BM presents the highest  $I_D/I_G$  ratio (and it is  $>1$ ), indicating that the amount of amorphous carbon is higher than the graphitic one, which is favourable for the stability of the catalyst since these species are more reactive, which is in agreement with the results obtained in the 24 h TOS experiments.

Operando NAP-XPS results highlight that the presence of Ru favours the  $\text{H}_2$  spillover and that the interaction between Ru and  $\text{CeO}_2$  is modified by the milling process, facilitating the formation of more oxygen vacancies in the ceria lattice thereby increasing its surface's reducibility, as seen in the table S7 with higher  $\text{Ce}^{4+}/\text{Ce}$  ratios for CoRu/ $\text{CeO}_2$ -BM catalyst. The NAP-XPS results of the mono- and bimetallic samples under reaction conditions correlate well with the catalytic measurements. Ruthenium is active in the activation of  $\text{CO}_2$  by dissociation of C-O bonds, thus making the bimetallic formulation more active in converting  $\text{CO}_2$ . This causes a stronger oxidation of cobalt species in bimetallic samples during reaction conditions, as observed for both synthesis methods in the low-temperature regime (550 °C). When the temperature increases to 700 °C, methane activation is strongly favoured leading to the reduction of cobalt. The effect of Ru addition and the synergy created between Co and Ru is also noticeable: in the IWI samples under reaction conditions at 700 °C, that is when the catalysts are more active, CoRu/ $\text{CeO}_2$ -IWI shows 30% CoO vs. 66% for Co/ $\text{CeO}_2$ -IWI, demonstrating that Ru helps in maintaining Co in a reduced state at this temperature. Checking the effect of the synthesis method, ball milling also promotes the reduction of Co species under DRM reaction conditions at 700 °C, which agrees with the TPR measurements and correlates with the catalytic performances obtained (Fig. 3). Remarkably, our results also reveal that the synthesis method has a clear effect on the Co reducibility, leading to the formation of different Co oxide species under reaction conditions: bimetallic catalysts show the formation of CoO for IWI-synthesized catalyst, while the mechanochemically-prepared one completely oxidized to  $\text{Co}_3\text{O}_4$ . Previous studies reported that at temperatures below 500 °C, cobalt is present in the form of CoO for the DRM reaction; here we show that the active Co species can be tuned with the synthesis method. This also indicates that the surface of the milled catalysts is more reactive and dynamic.

The NAP-XPS results revealed a different distribution of Ru on the surface of the BM that can indicate the presence of small Ru clusters that escape XRD detection and/or a distinct reorganization of Co and Ru that leads to Ru on top of Co. The higher Ru/(Ru+Co) ratio present on the surface could be responsible for the higher performance of the catalyst. The trend persists during DRM at 550 and 700 °C. Nevertheless, some sintering took place when increasing the reaction temperature, as the Ru/Ce reflects in CoRu/ $\text{CeO}_2$ -IWI (Table S10).

## 5. Conclusions

In this work, mono- and bimetallic CoRu/ $\text{CeO}_2$  catalysts were synthesized using two synthesis methods: a conventional incipient wetness impregnation (IWI) and a one-step mechanochemical process (ball-milling, BM). The mechanochemical synthesis resulted in an increased stability of the monometallic Co/ $\text{CeO}_2$  catalyst and  $\text{CH}_4$  and  $\text{CO}_2$  conversion of the ball-milled Ru/ $\text{CeO}_2$  sample by at least 10% compared to the IWI sample in all screened temperatures. Due to a shift in the position of the  $\text{RuO}_2$  peaks in the XRD results of the as-prepared Ru/ $\text{CeO}_2$  samples, it suggests a possible alloy of the Ru with part of the Co. The XRD results of Co/ $\text{CeO}_2$ -IWI and CoRu/ $\text{CeO}_2$ -IWI samples demonstrate that the addition of the noble metal leads to smaller metal particles, which enhances the activity. Ruthenium addition also altered the redox properties of BM and IWI Co-based catalysts, decreasing the temperature at which Co species underwent reduction. During the activity tests at 700 °C, the bimetallic catalysts reached higher  $\text{CH}_4$  and  $\text{CO}_2$  conversions and an  $\text{H}_2/\text{CO}$  ratio close to 1, proving the synergic effect between the

two metals. Stability tests were carried out and a stable performance for CoRu/CeO<sub>2</sub>-BM at 700 °C for 24 h was obtained. After the stability tests, Raman spectra revealed the presence of higher amounts of amorphous carbon in CoRu/CeO<sub>2</sub>-BM in contrast to the presence of higher amounts of graphitic carbon for CoRu/CeO<sub>2</sub>-IWI. These results clearly indicate that the synthesis method plays a major role in the catalysts' stability by conferring them with higher stability due to the formation of more reactive carbonaceous species. XRD results showed that Ru nanoparticles on CoRu/CeO<sub>2</sub>-IWI and -BM were of similar sizes. Nevertheless, NAP-XPS results showed a higher amount of Ru present on the surface of CoRu/CeO<sub>2</sub>-BM in comparison to the IWI counterpart, which can indicate the formation of small Ru clusters during the milling process, as confirmed from TEM analyses.

Remarkably, NAP-XPS results showed important differences in the reducibility of Co species and the CeO<sub>2</sub> support upon Ru addition. We proved that the presence of Ru facilitated the reduction of the support creating more oxygen vacancies for both synthesis methods. Besides, we revealed that the synthesis method also had a clear impact on the reducibility and rearrangement of the species during the DRM reaction. Cobalt species under reaction DRM conditions at 550 °C revealed different oxidation states depending on the synthesis method, being the BM catalysts more oxidized at lower temperatures due to a stronger ability to activate CO<sub>2</sub>. In the high-temperature regime (700 °C), the milled catalysts showed a higher reduction degree than the IWI counterparts, probably due to higher methane conversion. These results revealed that the surface of the milled catalysts is more reactive and dynamic than that of the traditionally synthesised counterparts. In this work, we show that by using a novel synthesis method, which is readily scalable for an industrial setting, active and stable Co/CeO<sub>2</sub>-based catalysts can be developed, overcoming one of their major drawbacks, which is their stability under time-on-stream.

#### CRediT authorship contribution statement

**Marina Armengol-Profitós:** Investigation, Methodology, Formal analysis, Writing – original draft. **Andrea Braga:** Investigation, Writing – review & editing. **Laia Pascua-Solé:** Investigation, Writing – review & editing. **Ilaria Lucentini:** Investigation, Writing – review & editing. **Xènia Garcia:** Investigation, Writing – review & editing. **Lluís Soler:** Investigation, Writing – review & editing. **Xavier Vendrell:** Investigation, Writing – review & editing. **Isabel Serrano:** Investigation, Writing – review & editing. **Ignacio J. Villar-García:** Investigation, Writing – review & editing. **Virginia Pérez-Dieste:** Investigation, Writing – review & editing. **Carlos Escudero:** Investigation, Writing – review & editing. **Núria J. Divins:** Conceptualization, Investigation, Methodology, Supervision, Validation, Writing – original draft, review & editing. **Jordi Llorca:** Conceptualization, Investigation, Supervision, Validation, Writing – review & editing, Funding acquisition.

#### Declaration of Competing Interest

The authors declare that they have no known competing financial interests or personal relationships that could have appeared to influence the work reported in this paper.

#### Data availability

All data will be made accessible upon reasonable request to the corresponding authors

#### Acknowledgements

This research was funded by MICINN/FEDER grant numbers PID2021-124572OB-C31 and PID2021-124572OB-C33, and by Generalitat de Catalunya grant number GC 2021 SGR 01061. M.A.-P. is grateful to 2020 FISDU 00219 grant from Generalitat de Catalunya. A.B.

is grateful to the European Union's H2020 Research and Innovation Program under the Marie Skłodowska-Curie grant agreement No. 813748. L.S.P. is grateful to 2022 FI\_B 00205 grant from Generalitat de Catalunya. L.S. is grateful to MICINN Ramon y Cajal Program for individual fellowship grant agreement RYC2019-026704-I. J.L. is a Serra Húnter Fellow and is grateful to the ICREA Academia Program. N.J.D. acknowledges the funding received from the European Union's Horizon 2020 research and innovation programme under the Marie Skłodowska-Curie grant agreement No 897197. Synchrotron XRD measurements were performed at MSPD (BL-04) and NOTOS (BL-16) beamlines and NAP-XPS measurements at CIRCE (BL-24) with the collaboration of ALBA Synchrotron staff. We are grateful to Dr. Carlos Frontera from Institut de Ciència de Materials de Barcelona (ICMAB).

#### Appendix A. Supporting information

Supplementary data associated with this article can be found in the online version at doi:10.1016/j.apcatb.2023.123624.

#### References

- [1] S.A. Theofanidis, H. Poelman, G.B. Marin, V.V. Galvita, How does the surface structure of ni-fe nanoalloys control carbon formation during methane steam/dry reforming? in: V.A. Sadykov (Ed.), in: Advanced Nanomaterials for Catalysis and Energy Elsevier, Amsterdam, 2019, pp. 177–225, <https://doi.org/10.1016/b978-0-12-814807-5.00006-1>.
- [2] IPCC, Climate Change 2007: Synthesis Report. Contribution of Working Groups I, II and III to the Fourth Assessment Report of the Intergovernmental Panel on Climate Change. 2007. <https://doi.org/10.1038/446727a>.
- [3] M. Boaro, S. Colussi, A. Trovarelli, Ceria-based materials in hydrogenation and reforming reactions for CO<sub>2</sub> valorization, *Front. Chem.* 7 (2019), <https://doi.org/10.3389/fchem.2019.00028>.
- [4] J.R.H. Ross, Natural gas reforming and CO<sub>2</sub> mitigation, *Catal. Today* 100 (2005) 151–158, <https://doi.org/10.1016/j.cattod.2005.03.044>.
- [5] M.S. Fan, A.Z. Abdullah, S. Bhatia, Catalytic technology for carbon dioxide reforming of methane to synthesis gas, *ChemCatChem* 1 (2009) 192–208, <https://doi.org/10.1002/cctc.200900025>.
- [6] S. Wang, G.Q. Lu, G. Millar, Carbon dioxide reforming of methane to produce synthesis gas over metal-supported catalysts: state of the art, *Energy Fuels* 10 (1996) 896–904, [https://doi.org/10.1016/0926-860X\(95\)00238-3](https://doi.org/10.1016/0926-860X(95)00238-3).
- [7] A.R. Puigdollers, P. Schlefer, S. Tosoni, G. Pacchioni, Increasing oxide reducibility: the role of metal/oxide interfaces in the formation of oxygen vacancies, in: ACS Catalysis, 7, American Chemical Society., 2017, pp. 6493–6513, <https://doi.org/10.1021/acscata.7b01913>.
- [8] K. Otsuka, E. Sunada, T. Ushiyama, I. Yamanaka, The production of synthesis gas by the redox of cerium oxide, *Stud. Surf. Sci. Catal.* 107 (1997) 531–536, [https://doi.org/10.1016/s0167-2991\(97\)80386-2](https://doi.org/10.1016/s0167-2991(97)80386-2).
- [9] N. Laosiripojana, S. Assabumrungrat, Catalytic dry reforming of methane over high surface area ceria, *Appl. Catal. B Environ.* 60 (2005) 107–116, <https://doi.org/10.1016/j.apcatb.2005.03.001>.
- [10] S.M. Kozlov, K.M. Neyman, Insights from methane decomposition on nanostructured palladium, *J. Catal.* 337 (2016) 111–121, <https://doi.org/10.1016/j.jcat.2016.02.010>.
- [11] M. Danielis, S. Colussi, C. de Leitenburg, L. Soler, J. Llorca, A. Trovarelli, Outstanding methane oxidation performance of palladium-embedded Ceria catalysts prepared by a one-step dry ball-milling method, *Angew. Chem. - Int. Ed.* 57 (2018) 10212–10216, <https://doi.org/10.1002/anie.201805929>.
- [12] A.P. Amrute, J. De Bellis, M. Felderhoff, F. Schütt, Mechanochemical synthesis of catalytic materials, *Chem. Eur. J.* 27 (2021) 6819–6847, <https://doi.org/10.1002/chem.202004583>.
- [13] P.M. Mortensen, I. Dybkjær, Industrial scale experience on steam reforming of CO<sub>2</sub>-rich gas, *Appl. Catal. A Gen.* 495 (2015) 141–151, <https://doi.org/10.1016/j.apcata.2015.02.022>.
- [14] S. Li, et al., Tuning the selectivity of catalytic carbon dioxide hydrogenation over iridium/cerium oxide catalysts with a strong metal-support interaction, *Angew. Chem.* 129 (2017) 10901–10905, <https://doi.org/10.1002/ange.201705002>.
- [15] C. Gennéquin, M. Safariamin, S. Siffert, A. Aboukais, E. Abi-Aad, CO<sub>2</sub> reforming of CH<sub>4</sub> over Co-Mg-Al mixed oxides prepared via hydrotalcite like precursors, *Catal. Today* 176 (2011) 139–143, <https://doi.org/10.1016/j.cattod.2011.01.029>.
- [16] D. Li, M. Lu, S. Xu, C. Chen, Y. Zhan, L. Jiang, Preparation of supported Co catalysts from Co-Mg-Al layered double hydroxides for carbon dioxide reforming of methane, *Int. J. Hydrog. Energy* 42 (2017) 5063–5071, <https://doi.org/10.1016/j.ijhydene.2016.10.114>.
- [17] C. Gennéquin, S. Kouassi, L. Tidahy, R. Cousin, J.F. Lamonier, G. Garcon, P. Shirali, F. Cazier, A. Aboukais, S. Siffert, Co-Mg-Al oxides issued of hydrotalcite precursors for total oxidation of volatile organic compounds. Identification and toxicological impact of the by-products, *C.R. Chim.* 13 (2010) 494–501, <https://doi.org/10.1016/j.crci.2010.01.001>.

[18] E. Ruckenstein, H.Y. Wang, Carbon deposition and catalytic deactivation during CO<sub>2</sub> reforming of CH<sub>4</sub> over Co- $\gamma$ -Al<sub>2</sub>O<sub>3</sub> catalysts, *J. Catal.* 205 (2002) 289–293, <https://doi.org/10.1006/jcat.2001.3458>.

[19] Y. Pang, A. Zhong, Z. Xu, W. Jiang, L. Gu, X. Feng, W. Ji, C.T. Au, How do core–shell structure features impact on the activity/stability of the co-based catalyst in dry reforming of methane? *ChemCatChem* 10 (2018) 2845–2857, <https://doi.org/10.1002/cctc.201800327>.

[20] J. Nakamura, K. Aikawa, K. Sato, T. Uchijima, Role of support in reforming of CH<sub>4</sub> with CO<sub>2</sub> over Rh catalysts, *Catal. Lett.* 25 (1994) 265–270, <https://doi.org/10.1007/BF00816306>.

[21] J.R. Rostrup-Nielsen, J.H. Bak Hansen, CO<sub>2</sub>-reforming of methane over transition metals, *J. Catal.* 144 (1993) 38–49, <https://doi.org/10.1006/jcat.1993.1312>.

[22] P. Ferreira-Aparicio, I. Rodríguez-Ramos, J.A. Anderson, A. Guerrero-Ruiz, Mechanistic aspects of the dry reforming of methane over ruthenium catalysts, *Appl. Catal. A Gen.* 202 (2000) 183–196, [https://doi.org/10.1016/S0926-860X\(00\)00525-1](https://doi.org/10.1016/S0926-860X(00)00525-1).

[23] R. Mahfouz, J. Estephane, C. Gennequin, L. Tidahy, S. Aouad, E. Abi-Aad, CO<sub>2</sub> reforming of methane over Ni and/or Ru catalysts supported on mesoporous KIT-6: effect of promotion with Ce, *J. Environ. Chem. Eng.* 9 (1) (2021) 9, <https://doi.org/10.1016/j.jece.2020.104662>.

[24] Z. Liu, F. Zhang, N. Rui, X. Li, L. Lin, L.E. Betancourt, D. Su, W. Xu, J. Cen, K. Attenkofer, H. Idriss, J.A. Rodriguez, S.D. Senanayake, Highly active Ceria-supported Ru catalyst for the dry reforming of methane: in situ identification of Ru<sup>+</sup>–Ce<sup>3+</sup> interactions for enhanced conversion, *ACS Catal.* 9 (2019) 3349–3359, <https://doi.org/10.1021/acscatal.8b05162>.

[25] K. Nagaoka, K. Takanabe, K. Aika, Modification of Co/TiO<sub>2</sub> for dry reforming of methane at 2 MPa by Pt, Ru or Ni, *Appl. Catal. A Gen.* 268 (2004) 151–158, <https://doi.org/10.1016/j.apcata.2004.03.029>.

[26] M. Myint, B. Yan, J. Wan, S. Zhao, J.G. Chen, Reforming and oxidative dehydrogenation of ethane with CO<sub>2</sub> as a soft oxidant over bimetallic catalysts, *J. Catal.* 343 (2016) 168–177, <https://doi.org/10.1016/j.jcat.2016.02.004>.

[27] W. Tu, M. Ghoussoub, C.V. Singh, Y.-H.C. Chin, Consequences of surface oxophilicity of Ni, Ni-Co, and Co clusters on methane activation, *J. Am. Chem. Soc.* 139 (2017) 6928–6945, <https://doi.org/10.1021/jacs.7b01632>.

[28] Z. Xie, B. Yan, S. Kattel, J.H. Lee, S. Yao, Q. Wu, N. Rui, E. Gomez, Z. Liu, W. Xu, L. Zhang, J.G. Chen, Dry reforming of methane over CeO<sub>2</sub>-supported Pt-Co catalysts with enhanced activity, *Appl. Catal. B Environ.* 236 (2018) 280–293, <https://doi.org/10.1016/j.apcatb.2018.05.035>.

[29] M.A. Álvarez, L.F. Bobadilla, V. Garcilaso, M.A. Centeno, J.A. Odriozola, A.Á. M., L. F. Bobadilla, V. Garcilaso, M.A. Centeno, J.A. Odriozola, CO<sub>2</sub> reforming of methane over Ni-Ru supported catalysts: on the nature of active sites by operando DRIFTS study, *J. CO<sub>2</sub> Util.* 24 (2018) 509–515, <https://doi.org/10.1016/j.jcou.2018.01.027>.

[30] A. Álvarez Moreno, T. Ramirez-Reina, S. Ivanova, A.C. Roger, M.Á. Centeno, J. A. Odriozola, Bimetallic Ni–Ru and Ni–Re catalysts for dry reforming of methane: understanding the synergies of the selected promoters, *Front. Chem.* 9 (2021) 1–10, <https://doi.org/10.3389/fchem.2021.694976>.

[31] L.A. Bruce, M. Hoang, A.E. Hughes, T.W. Turney, Ruthenium promotion of Fischer-Tropsch synthesis over coprecipitated cobalt/ceria catalysts, *Appl. Catal. A Gen.* 100 (1993) 51–67, [https://doi.org/10.1016/0926-860X\(93\)80115-7](https://doi.org/10.1016/0926-860X(93)80115-7).

[32] A. Trovarelli, F. Zamar, J. Llorca, C. de Leitenburg, G. Dolcetti, J.T. Kiss, Nanophase fluorite-structured CeO<sub>2</sub>–ZrO<sub>2</sub> catalysts prepared by high-energy mechanical milling, *J. Catal.* 169 (1997) 490–502, <https://doi.org/10.1006/jcat.1997.1705>.

[33] Y. Chen, L. Soler, M. Armengol-Profitós, C. Xie, D. Crespo, J. Llorca, Enhanced photoproduction of hydrogen on Pd/TiO<sub>2</sub> prepared by mechanochemistry, *Appl. Catal. B Environ.* 309 (2022) 121275, <https://doi.org/10.1016/j.apcatb.2022.121275>.

[34] K. Ralphs, C. Hardacre, S.L. James, Application of heterogeneous catalysts prepared by mechanochemical synthesis, *Chem. Soc. Rev.* 42 (2013) 7701–7718, <https://doi.org/10.1039/c3cs60066a>.

[35] E. Aneggi, V. Rico-Perez, C. de Leitenburg, S. Maschio, L. Soler, J. Llorca, A. Trovarelli, Ceria-Zirconia particles wrapped in a 2D carbon envelope: improved low-temperature oxygen transfer and oxidation activity, *Angew. Chem. Int. Ed.* 54 (2015) 14040–14043, <https://doi.org/10.1002/anie.201507839>.

[36] A. Mussio, M. Danielis, N.J. Divins, J. Llorca, S. Colussi, A. Trovarelli, Structural evolution of bimetallic PtPd/CeO<sub>2</sub> methane oxidation catalysts prepared by dry milling, *ACS Appl. Mater. Interfaces* 13 (2021) 31614–31623, <https://doi.org/10.1021/acsmami.1c05050>.

[37] N.J. Divins, A. Braga, X. Vendrell, I. Serrano, X. Garcia, L. Soler, I. Lucentini, M. Danielis, A. Mussio, S. Colussi, I.J. Villar-Garcia, C. Escudero, A. Trovarelli, J. Llorca, Investigation of the evolution of Pd–Pt supported on ceria for dry and wet methane oxidation, *Nat. Commun.* 13 (1) (2022) 11, <https://doi.org/10.1038/s41467-022-32765-4>.

[38] J.D. Jiménez, L.E. Betancourt, M. Danielis, H. Zhang, F. Zhang, I. Orozco, W. Xu, J. Llorca, P. Liu, A. Trovarelli, J.A. Rodriguez, S. Colussi, S.D. Senanayake, Identification of highly selective surface pathways for methane dry reforming using mechanochemical synthesis of Pd-CeO<sub>2</sub>, *ACS Catal.* 12 (2022) 12809–12822, <https://doi.org/10.1021/acscatal.2c01120>.

[39] J.M. Pan, X.J. Wei, Determination of ruthenium in waste ruthenium catalysts using inductively coupled plasma optical emission spectrometry after sample digestion by high temperature fusion, *Adv. Mater. Res.* 1033–1034 (2014) 603–606, <https://doi.org/10.4028/www.scientific.net/AMR.1033-1034.603>.

[40] E. Béche, P. Charvin, D. Perarnau, S. Abanades, G. Flamant, Ce 3d XPS investigation of cerium oxides and mixed cerium oxide (Ce<sub>x</sub>Ti<sub>y</sub>O<sub>2</sub>), *Surf. Interface Anal.* 40 (2008) 264–267, <https://doi.org/10.1002/sia.2686>.

[41] A.P. Grosvenor, S.D. Wik, R.G. Cavell, A. Mar, Examination of the bonding in binary transition-metal monophosphides MP (M = Cr, Mn, Fe, Co) by X-ray photoelectron spectroscopy, *Inorg. Chem.* 44 (2005) 8988–8998, <https://doi.org/10.1021/ic051004d>.

[42] M. Domínguez, E. Taboada, H. Idriss, E. Molins, J. Llorca, Fast and efficient hydrogen generation catalyzed by cobalt tale nanolayers dispersed in silica aerogel, *J. Mater. Chem.* 20 (2010) 4875–4883, <https://doi.org/10.1039/c0jm00184h>.

[43] N.J. Divins, I. Angurell, C. Escudero, V. Pérez-Dieste, J. Llorca, Influence of the support on surface rearrangements of bimetallic nanoparticles in real catalysts, *Science* 346 (2014) 620–623, <https://doi.org/10.1126/science.1258106>.

[44] D.J. Morgan, Resolving ruthenium: XPS studies of common ruthenium materials, *Surf. Interface Anal.* 47 (2015) 1072–1079, <https://doi.org/10.1002/sia.5852>.

[45] Y.J. Kim, Y. Gao, S.A. Chambers, Core-level X-ray photoelectron spectra and X-ray photoelectron diffraction of RuO<sub>2</sub>(110) grown by molecular beam epitaxy on TiO<sub>2</sub>(110), *Appl. Surf. Sci.* 120 (1997) 250–260, [https://doi.org/10.1016/S0169-4332\(97\)00233-X](https://doi.org/10.1016/S0169-4332(97)00233-X).

[46] R. Pugliese, G. Paolucci, Atomic calculation of photoionization cross-sections and asymmetry parameters, 2022. <https://vuo.elettra.eu/services/elements/WebElements.html>.

[47] G. Bergeret, P. Gallezot, Particle size and dispersion measurements, in: *Handbook of Heterogeneous Catalysis*, 2008.

[48] C.W. Tang, C. Bin Wang, S.H. Chien, Characterization of cobalt oxides studied by FT-IR, Raman, TPR and TG-MS, *Thermochim. Acta* 473 (2008) 68–73, <https://doi.org/10.1016/j.tca.2008.04.015>.

[49] F. Giordano, A. Trovarelli, C. De Leitenburg, M. Giona, A model for the temperature-programmed reduction of low and high surface area Ceria, *J. Catal.* 193 (2000) 273–282, <https://doi.org/10.1006/jcat.2000.2900>.

[50] J. Sasson Bitters, T. He, E. Nestler, S.D. Senanayake, J.G. Chen, C. Zhang, Utilizing bimetallic catalysts to mitigate coke formation in dry reforming of methane, *J. Energy Chem.* 68 (2022) 124–142, <https://doi.org/10.1016/j.jecchem.2021.11.041>.

[51] F. Zhang, et al., In situ elucidation of the active state of Co–CeO<sub>x</sub> catalysts in the dry reforming of methane: the important role of the reducible oxide support and interactions with cobalt, *ACS Catal.* 8 (2018) 3550–3560, <https://doi.org/10.1021/ACSCATAL.7B03640>.

[52] C. Huck-Iriart, L. Soler, A. Casanovas, C. Marini, J. Prat, J. Llorca, C. Escudero, Unraveling the chemical state of cobalt in co-based catalysts during ethanol steam reforming: an in situ study by near ambient pressure XPS and XANES, *ACS Catal.* 8 (2018) 9625–9636, <https://doi.org/10.1021/acscatal.8b02666>.

[53] K. Jabbour, N. El Hassan, S. Casale, J. Estephane, H. El Zakhem, Promotional effect of Ru on the activity and stability of Co/SBA-15 catalysts in dry reforming of methane, *Int. J. Hydrol. Energy* 39 (2014) 7780–7787, <https://doi.org/10.1016/j.ijhydene.2014.03.040>.

[54] F. Zhang, et al., In situ elucidation of the active state of Co–CeO<sub>x</sub> catalysts in the dry reforming of methane: the important role of the reducible oxide support and interactions with cobalt, *ACS Catal.* 8 (2018) 3550–3560, <https://doi.org/10.1021/acscatal.7b03640>.

[55] A.W. Budiman, S.H. Song, T.S. Chang, C.H. Shin, M.J. Choi, Dry reforming of methane over cobalt catalysts: a literature review of catalyst development, *Catal. Surv. Asia* 16 (2012) 183–197, <https://doi.org/10.1007/s10563-012-9143-2>.

[56] A. Pappacena, R. Razzaq, C. de Leitenburg, M. Boaro, A. Trovarelli, The role of neodymium in the optimization of a Ni/CeO<sub>2</sub> and Ni/CeZrO<sub>2</sub> Methane dry reforming catalyst, *Inorganics* 6 (2018) 1–15, <https://doi.org/10.3390/inorganics6020039>.

[57] N. Wang, W. Qian, W. Chu, F. Wei, Crystal-plane effect of nanoscale CeO<sub>2</sub> on the catalytic performance of Ni/CeO<sub>2</sub> catalysts for methane dry reforming, *Catal. Sci. Technol.* 6 (2016) 3594–3605, <https://doi.org/10.1039/c5cy01790d>.

[58] I. Luisetto, S. Tuti, E. Di Bartolomeo, Co and Ni supported on CeO<sub>2</sub> as selective bimetallic catalyst for dry reforming of methane, *Int. J. Hydrol. Energy* 37 (2012) 15992–15999, <https://doi.org/10.1016/j.ijhydene.2012.08.006>.

[59] B.C. Enger, R. Lødeng, A. Holmen, Effects of noble metal promoters on in situ reduced low loading Ni catalysts for methane activation, *Catal. Lett.* 134 (2010) 13–23, <https://doi.org/10.1007/s10562-009-0219-1>.

[60] C. Wang, T. Su, Z. Qin, H. Ji, Coke-resistant Ni-based bimetallic catalysts for the dry reforming of methane: effects of indium on the Ni/Al<sub>2</sub>O<sub>3</sub> catalyst, *Catal. Sci. Technol.* 12 (2022) 4826–4836, <https://doi.org/10.1039/d2cy00582d>.